

Ultrafast Laser Spectroscopy of Half-Metallic Chromium
Dioxide

A Dissertation

Presented to

The Faculty of the Department of Physics
The College of William & Mary in Virginia

In Partial Fulfillment

Of the Requirements for the Degree of

Doctor of Philosophy

by

Hailong Huang

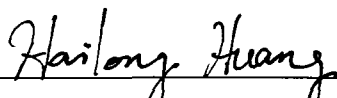
2006

APPROVAL SHEET

This dissertation is submitted in partial fulfillment of

the requirements for the degree of

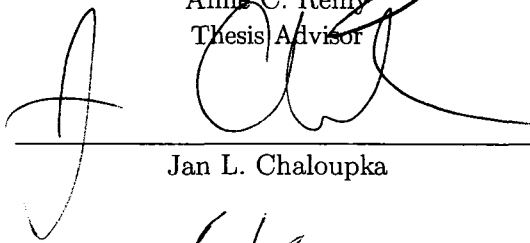
Doctor of Philosophy


Hailong Huang

Approved, February 6, 2006



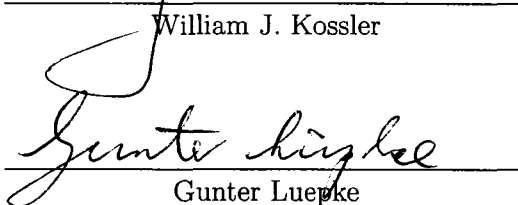
Anna C. Reilly
Thesis Advisor



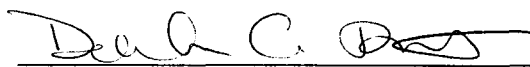
Jan L. Chaloupka



William J. Kossler



Gunter Luepke
Department of Applied Science



Deborah C. Bebout
Department of Chemistry

To my parents . . .

Table of Contents

| | |
|--|-------------|
| Acknowledgements | viii |
| List of Tables | ix |
| List of Figures | x |
| Abstract | xiii |
| 1 Introduction | 2 |
| 1.1 Review of the Ultrafast Laser Experiments in Magnetic Materials and Half Metals | 6 |
| 1.2 Outline of Thesis | 7 |
| 2 Review of Properties of Half-Metallic Chromium Dioxide | 9 |
| 2.1 General Types and Properties of Half Metals | 10 |
| 2.2 CrO ₂ | 14 |
| 2.2.1 Introduction | 14 |
| 2.2.2 Theoretical Bandstructure Calculations | 16 |
| 2.2.3 Spin Resolved Photo Emission and PCAR | 18 |

| | | |
|----------|---|-----------|
| 2.2.4 | Critical Behavior | 19 |
| 2.2.5 | Transport Measurements | 19 |
| 2.2.6 | Optical Spectroscopy Study | 20 |
| 2.2.7 | Orbital Moments | 21 |
| 2.2.8 | Magnetic Measurements | 22 |
| 3 | Theory of Ultrafast Laser Pump-Probe Spectroscopy and MOKE | 24 |
| 3.1 | Ultrafast pump-probe spectroscopy | 24 |
| 3.2 | Magneto-optical Kerr Effect (MOKE) | 29 |
| 3.3 | Incoherent and Coherent Magnetization Dynamics | 34 |
| 3.4 | Magnetization Dynamics | 35 |
| 3.5 | FMR Analysis of the LLG | 38 |
| 4 | Experimental Methods | 40 |
| 4.1 | Ultrafast Pump-probe Experiment | 40 |
| 4.2 | Static Magneto-Optical Kerr Effect (MOKE) Experiment | 44 |
| 4.3 | Ultrafast MOKE Experiments | 46 |
| 4.4 | Sample Preparation and Characterization | 47 |
| 5 | Ultrafast Spectroscopy of CrO₂ | 52 |
| 5.1 | Background | 52 |
| 5.2 | Experiment | 54 |
| 5.3 | Results and Discussion | 55 |
| 5.4 | Summary | 63 |

| | |
|---|------------|
| 6 Spin Lifetimes of CrO₂ Probed by Ultrafast MOKE | 64 |
| 6.1 Introduction | 65 |
| 6.2 Experiment | 66 |
| 6.3 Results | 67 |
| 6.4 Summary | 72 |
| 7 Coherent Magnetization Oscillation in CrO₂ and Temperature Dependent Study of Magnetic Anisotropy | 74 |
| 7.1 Background | 75 |
| 7.2 Experiment | 78 |
| 7.3 Room temperature anisotropy measurement | 80 |
| 7.4 Temperature dependent study of anisotropy | 87 |
| 7.5 Summary | 92 |
| 8 Conclusion | 95 |
| A Spectra Physics Laser Systems | 97 |
| A.1 Tsunami | 97 |
| A.2 Spitfire | 98 |
| A.3 OPA-800C | 98 |
| B Fortran Programs | 100 |
| B.1 Data Fitting | 100 |
| B.2 Recovering | 107 |

| | |
|---------------------|------------|
| Bibliography | 110 |
| Vita | 117 |

ACKNOWLEDGEMENTS

First, I want to thank my advisor Prof. Anne Reilly. I wish I could find the proper word to express my appreciation for what she has done to help me in the past five years, both with my research and with my career. Her knowledge, enthusiasm and scientific integrity have always been beneficial to me. This work would not have been possible without her tremendous support.

I want to thank our collaborators, Prof. William Egelhoff from the National Institute of Standards and Technology (NIST), and Prof. Ale Lukaszew from the University of Toledo. They provided the samples in this work as well as much of the characterization data.

My sincere gratitude goes to the committee members, Prof. Gunter Luepke, Prof. William Kossler, Prof. Jan Chaloupka, and Prof. Deborah Bebout. Their time and effort has been highly appreciated.

I also valued the experimental support of Martin Hou, Qiguang Yang, Shannon Watson, Wei Yang, Wendy Vogan, and Xin Zhao. Great or small, their help has been invaluable, even though some may not remember their contribution.

A special thanks for Keoki Seu, my research group mate, office mate, and computer guru. Without him the programming of this endeavor would have proved to be more taxing.

Prof. Yuhang Ren of Hunter College has continually supported me even as he was a student himself at the College of William and Mary. I not only appreciate his aid but his friendship as well.

I sincerely appreciated the support of my roommates Haibin Zhao and Rui Yang. They are wonderful, and have been like family to me.

I want to thank my friends from church from both here in Williamsburg and in Newport News. They made my life here at William and Mary equally enjoyable and memorable.

Finally, I want to thank my parents for their incessant love and support. Thanks is definitely due especially considering the fact that they were cooking for me during the last few months which allowed me more time to write up this thesis.

List of Tables

| | | |
|-----|---|----|
| 2.1 | Types of half-metals | 11 |
| 2.2 | Measured spin polarizations of some materials using PCAR | 13 |
| 2.3 | Experimental methods of spin polarization measuring | 14 |
| 2.4 | Theoretical calculation of CrO ₂ band structure | 17 |
| 7.1 | Comparison of our results with other measurements of anisotropy | 86 |
| 7.2 | Error analysis | 91 |
| 7.3 | Extracted values for uniaxial and strain anisotropy as a function of temperature | 92 |

List of Figures

| | | |
|-----|--|----|
| 1.1 | Magnetic Tunnel Junction | 3 |
| 2.1 | Point Contact Andreev Reflection | 12 |
| 2.2 | Crystal Structure of CrO ₂ | 15 |
| 2.3 | Band Structure of CrO ₂ | 16 |
| 2.4 | Spin Resolved DOS of CrO ₂ | 21 |
| 3.1 | Pump-Probe Experiment Setup | 25 |
| 3.2 | Three Temperature Model | 30 |
| 3.3 | MOKE Configuration | 30 |
| 3.4 | The Motion of Magnetic Moment | 36 |
| 4.1 | Ultrafast Pump-probe Setup | 40 |
| 4.2 | MOKE Setup and a Typical Hysteresis Loop | 44 |
| 4.3 | Schematic of a Balanced Detector | 45 |
| 4.4 | Ultrafast MOKE Setup | 47 |
| 4.5 | Hysteresis Loops of CrO ₂ Samples | 48 |
| 4.6 | The Optical Absorption Result | 49 |

| | | |
|-----|---|----|
| 4.7 | Coercivity versus Applied Field Angle | 51 |
| 5.1 | Pump-probe Differential Transmission at 300 K | 56 |
| 5.2 | Pump-probe Differential Transmission at Various Temperatures | 59 |
| 5.3 | Behavior of the differential absorption as a function of temperature | 60 |
| 5.4 | Schematic of the Density of States (DOS) Near the Fermi Surface | 61 |
| 6.1 | Ultrafast MOKE Setup | 66 |
| 6.2 | Dynamic MOKE Signal for Various Delay Times | 67 |
| 6.3 | Ultrafast MOKE Results | 68 |
| 6.4 | Differential MOKE Curves | 69 |
| 6.5 | Differential Transmission Signals Fit with Single Decay Component | 71 |
| 6.6 | Differential Transmission Signals Fit with Two Decay Components | 71 |
| 6.7 | The Temperature Dependence of the Relaxation Times | 73 |
| 7.1 | Generation of Coherent Magnetization Oscillations | 77 |
| 7.2 | SEM Image | 79 |
| 7.3 | Hysteresis Loops | 79 |
| 7.4 | Coherent Magnetization Oscillation | 81 |
| 7.5 | Numerical Fitting | 85 |
| 7.6 | Low Temperature Oscillations | 87 |
| 7.7 | Coherent Magnetization Oscillations as a Function of Temperature and Field | 88 |

| | |
|--|----|
| 7.8 Oscillation Frequencies as a Function of Applied Field at High Temperatures | 89 |
| 7.9 Oscillation Frequencies as a Function of Applied Field at Low Temperatures | 90 |
| 7.10 Error Analysis | 90 |
| 7.11 Values for Uniaxial Anisotropy and Strain Anisotropy as a Function of Temperature | 93 |
| A.1 Spectra-Physics Tsunami | 97 |
| A.2 Spectra-Physics Spitfire | 98 |
| A.3 Spectra-Physics OPA-800C | 99 |

ABSTRACT

This thesis presents ultrafast laser pump-probe differential transmission experiments on epitaxial CrO₂ (110). The experiments were conducted at the wavelengths of 600 nm, 800 nm and 1200 nm, corresponding to the transition energies of 2 eV, 1.5 eV and 1 eV respectively. The wavelength dependent results, comparing with linear optical absorption, revealed the electronic structure of the material. The experimental results also showed polarization dependence of the probe beams. This is attributed to the electronic orbital anisotropy.

Temperature dependence was observed in the pump-probe experiments. The ultrafast transmission data show similar temperature dependence as ultrafast MOKE (Magneto-Optical Kerr Effect) data. A critical change of transient transmission was observed at the Curie temperature of 386 K. Spin decay processes are discussed based on these temperature dependent time resolved data.

Ultrafast MOKE experiments are also presented. Oscillations of the time resolved MOKE signal corresponding to the ferromagnetic resonance were observed. The magnetic anisotropies of the CrO₂ thin film were studied by analyzing these oscillations. A computer program was developed for data analysis.

A general discussion of the relation between magnetic properties and the electronic properties of the material is delivered.

Ultrafast Laser Spectroscopy of Half-Metallic Chromium
Dioxide

Chapter 1

Introduction

Chromium dioxide, CrO_2 , a ferromagnetic metal which has long been used as tape recording media, has recently attracted much attention due to its half-metallic properties [1, 2, 3]. A half metallic material has a vastly different bandstructure for the two electron spin types (up or down). For the majority electron spins, the bandstructure is metallic. For the minority spins, however, there is a significant gap around the Fermi level, and these spins have a low density of states at the Fermi level. This means that the spin polarization at the Fermi level approaches 100%, and that electrical conduction through a half metal takes place by primarily one spin type. The half-metallic property of CrO_2 deeply affects the transport properties of the material and makes it a potential candidate for spintronic devices and spin injectors [4, 5].

In spintronics, the spins of the carriers become a new degree of freedom, in contrast to conventional electronic devices, which rely only on the transport of the charged carriers. Information can be stored in the spin states of the carriers, which can be considered as “0” and “1” in information terminology, and delivered to the terminals by electronic current. Half-metals have very broad application in this area.

A relatively simple and yet important spintronic device is a magnetic tunnel junc-

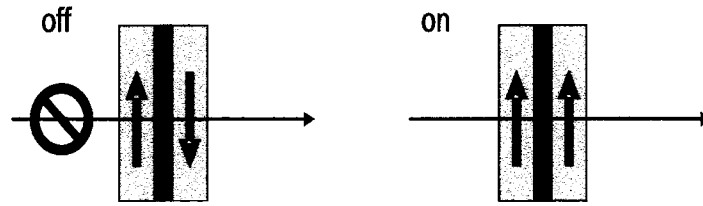


Figure 1.1: A magnetic tunnel junction

tion, shown in Figure 1.1. Two layers of magnetic metals are connected by an insulating layer. When the magnetic moments of the two metallic layers are parallel, the electrical resistance of the device is small because the majority spins of one metallic layer can tunnel through the insulating barrier and become the majority spins of another metallic layer. When the magnetic moments of the two metallic layers are anti-parallel, the majority spins of one metallic layer have to tunnel through the insulating barrier and become the minority spins and vice versa, and thus the electrical resistance is high. An external magnetic field can be applied to control the electrical resistance of the device. The relative change of the resistance due to the external field is called magneto-resistance (MR). Even 5% MR is useful in magnetic recording. The tunneling magnetoresistance is related to the spin polarization of the magnetic material according to Julliere's formula [6]:

$$MR = \frac{2P^2}{1 - P^2} \quad (1.1)$$

where P is the spin polarization of the two layers, with the spin polarization defined as:

$$P = (N \uparrow - N \downarrow) / (N \uparrow + N \downarrow) \quad (1.2)$$

N refers to the density of states of the spin up and spin down electrons, respectively. It can be seen from the above formula for MR that as the spin polarization approaches 100% (or 1), the MR would increase infinitely, which means the electrical current through the device can be totally cut off if the magnetic moments of the two half-metallic layers are anti-parallel [7]. This large enhancement of MR is of extreme interest for technological applications, such as magnetic recording and sensing.

Although a significant amount of theoretical and experimental work has been done attempting to identify half-metallic materials and incorporate them successfully into devices, the very large enhancements expected in magnetoresistance have yet to be realized. Part of the problem has been the difficulty in producing materials with the theoretically predicted spin polarizations, accurately measuring the polarizations, and preserving the spin polarization when the half-metallic material is included in a multilayer structure (where rough interfaces could destroy the spin polarization). However, interest in half metals still remains because of their great potential.

One major issue has been developing a reliable and easy way to identify a half metal. The most straightforward way is to measure the spin polarization, which can be done by several techniques such as spin-resolved photoemission and Point Contact Andreev Reflection. These techniques either require ultra high vacuum environments or low temperatures and are surface sensitive, so they are not widely applicable. Another way to measure the spin polarization is to construct a magnetic tunnel junction, but one would like to know beforehand if a material is a promising candidate for half-metallic behavior before going through the difficulty of producing a device. An-

other separate issue for spintronics applications is the measurement of spin dynamics and lifetimes in materials, as this would affect the ultimate speed at which magnetic devices could be operated.

Ultrafast laser spectroscopy (employing lasers with pulses lasting from tens of femtoseconds to picoseconds) has been applied to a wide range of materials to elucidate information on dynamics and energy dependent structure. In particular, ultrafast spectroscopy has been a powerful tool for learning about electron dynamics in semiconductors [8, 9] and metals [10]. Most recently, ultrafast techniques have been modified and used to learn about spin and magnetization dynamics in magnetic materials. These experiments have opened up new opportunities to learn about the ultimate timescales of magnetic processes [11, 12, 13].

The simplest type of ultrafast laser experiment is the pump-probe experiment. In this technique, a sample is hit by a pump pulse, and an excited state is created. A probe pulse, delayed in time through an additional optical path, hits the sample and is reflected by or transmitted through the sample. The information of the excited states of the sample is found by measuring the reflected or transmitted probe pulse. The essence of the pump-probe technique is it takes a “snap shot” of what happens in a very short time period. It is a direct optical method for studying dynamic processes. The pump-probe experiment is a typical method of studying the materials in their excited states and a direct way of measuring the lifetime of many types of excitations [14].

This dissertation presents a study of the application of ultrafast pump-probe laser

spectroscopy the aim of which was to learn about the electron and spin dynamics in half-metallic CrO₂. Specifically, we set out on this study to determine if there are unique optical signatures which indicate the half-metallic nature of CrO₂ and what unique features of the electron and spin dynamics we could learn through ultrafast laser spectroscopy.

1.1 Review of the Ultrafast Laser Experiments in Magnetic Materials and Half Metals

Ultrafast pump-probe techniques have been recently applied to learn about magnetic dynamics in metals. The first experiment, conducted in 1996, showed that the magnetization could be directly perturbed by an ultrafast laser pulse, and the relaxation measured through the probe transmission and the magneto-optical Kerr effect [15, 16]. More recent experiments showed that the pump laser pulses could modify magneto-crystalline [13] or artificially introduced anisotropy [17] (exchange biasing), leading to coherent magnetization oscillations. In another class of experiments, an ultrafast laser pulse was used to activate an optical switch which produced an ultrafast magnetic field pulse that perturbs the magnetization. Coherent magnetization precession were detected using ultrafast laser pulses delayed in time, using the Faraday or magneto-optical Kerr effect (MOKE) [18, 19].

There have only been a few studies applying the pump-probe technique to half metals. In 2000, Kise et al. reported on ultrafast MOKE study of half-metallic

SrFe₂MoO₆ [11]. The spin relaxation time was found to be slow but temperature dependent; In 2002, Zhang et al. reported on pump-probe study of half-metallic CrO₂, and produced coherent magnetization oscillations in the material [12]. There remain many opportunities to learn about dynamics of a multitude of half metals by ultrafast laser techniques.

1.2 Outline of Thesis

The whole thesis is divided into eight chapters. Chapter 1 is the review of this dissertation. Chapter 2 presents an introduction to the half-metallic materials, especially half-metallic CrO₂, focusing on their properties and applications. Chapter 3 presents basic theories of laser-material interactions, including the magneto-optical Kerr effect (MOKE), ultrafast laser pump-probe experiments and the electronic and spin decay processes after the laser pumping. Chapter 4 describes the experimental setups used for this thesis work and briefly outlines the production and characterization of the thin films used for this work.

Chapter 5 presents results of an ultrafast laser pump-probe study of electron and spin dynamics as revealed through the probe transmission. The study is conducted at several different wavelengths (energies) for the probe beam, corresponding to prominent features in the absorption spectrum of CrO₂. Optical anisotropy was observed, which is consistent with current bandstructure models for CrO₂. The wavelength and temperature dependent measurements imply there is a band gap of 1.5 ~ 2 eV near the Fermi surface, consistent with recent calculations. This Chapter presents data

which shows that important features of bandstructure and magnetization of CrO_2 can be studied using ultrafast transmission experiments.

Chapter 6 presents results of magnetization dynamics as measured through the pump-probe magneto-optical Kerr effect. Dynamics similar to those seen in the half-metal $\text{SrFe}_2\text{MoO}_6$ will be presented. The measurements presented in this Chapter are the first to show that the magnitude of magnetization of CrO_2 can be directly modified by an ultrafast pump, much like Ni [15].

Chapter 7 presents results of a study of coherent magnetization dynamics as measured by pump-probe MOKE. Coherent oscillations similar to those seen by Nurmikko's group are presented [12]. We extend their study across a wide range of temperatures. Results presented in this Chapter show that the ultrafast MOKE technique can be used to extract values for magnetocrystalline anisotropy which are consistent with other types of measurements. The temperature dependent data show a unique feature at low temperature. Chapter 8 summarizes the thesis and presents suggestions for future experiments.

Chapter 2

Review of Properties of Half-Metallic Chromium Dioxide

Some of the first materials which were suggested theoretically to be half-metallic are the Heusler alloys (e.g. NiMnSb and PtMnSb). Initial interest in Heusler alloys was generated by the fact that these compounds are strongly ferromagnetic although they are made by combining some elements that are considered nonmagnetic. Theoretical calculations were performed to explore the electronic and magnetic properties of these materials. In 1983, R. A. de Groot and coworkers calculated the band structure of face-centered cubic (fcc) Heusler alloys NiMnSb and PtMnSb using the augmented-spherical-wave method [20]. Surprisingly, they found that in NiMnSb there is a clear gap at the Fermi level for the minority spin electrons, although for the electrons with majority spins the material is metallic. This electronic configuration causes 100% spin polarization at the Fermi level. The spin polarization of PtMnSb was also found to be very high. The half-metallic behavior of NiMnSb was confirmed by later calculations and experiments.

In 1986, a totally different type of material, chromium dioxide, was predicted as a half-metal using the same augmented-spherical-wave method [1]. The result was soon confirmed by spin-polarized photoemission a year later [2]. Intensive theoret-

ical calculations [21, 22, 23, 24] and experimental explorations [25, 26, 3, 27, 28] followed to study this new type of half-metallic material because of its simplicity in lattice structure and novelty in electronic and magnetic properties.

2.1 General Types and Properties of Half Metals

Half-metals are not limited to these two types of materials. Many other half-metallic materials of different lattice structures were found in the later years. These materials include spinels (e.g. Fe_3O_4), Perovskites manganites (e.g. $\text{La}_{1-x}\text{Sr}_x\text{MnO}_3$ and $\text{La}_{1-x}\text{Ca}_x\text{MnO}_3$), double Perovskites oxides (e.g. $\text{Sr}_2\text{Fe-MoO}_6$), materials of zinc-blende structure (e.g. MnSb and MnBi), pyrites (e.g. CoS_2) and some dilute magnetic semiconductors (e.g. $\text{Ga}_{1-x}\text{Mn}_x\text{As}$ and $\text{Hg}_{1-x}\text{Mn}_x\text{MnSe}$). Table 2.1 is a list of the types of half-metals and related references.

Some of these materials, like CrO_2 and $\text{La}_{0.7}\text{Sr}_{0.3}\text{MnO}_3$ thin films, have been experimentally verified at low temperature to have near 100% spin polarization at the Fermi surface [3, 34]. But the spin polarizations of these materials reduce much quicker than their magnetizations at increased temperature [41, 42]. As a result, Heusler alloys, zinc-blende ferromagnets and magnetite, although they have been shown to have a lower spin polarization, have seen more application in device design due to their high Curie temperatures [43]. Zinc-blende ferromagnets have been theoretically predicted to be half-metallic under certain conditions [36], but no experiment to date has verified these predictions.

There is not a universal experimental method to check if a material is half-metal.

| samples | theoretical prediction | experimental verification |
|--|------------------------|---|
| Heusler Alloys: NiMnSb | Ref [20] | positron annihilation, Ref [29] |
| Binary Oxides: CrO ₂ | Ref [1] | PCAR, Ref [3] spin resolved PEM, Ref [27] |
| Spinels: Fe ₃ O ₄ | Ref [30] | spin resolved PEM, Ref [31] |
| Perovskite Manganites: La _{0.7} Sr _{0.3} MnO ₃ La _{0.7} Ca _{0.3} MnO ₃ | Ref [32] | PCAR, Ref [33] spin resolved PEM, Ref [34] |
| Double Perovskite Oxides: Sr ₂ FeMnO ₆ | Ref [35] | |
| Zinc-Blende Structure: MnAs, MnBi | Ref [36] | |
| Pyrite Alloys: Fe _{1-x} Co _x S ₂ | Ref [37] | PCAR, Ref [38] |
| Dilute Magnetic Semiconductors: Ga _{1-x} Mn _x As | Ref [39] | PCAR, Ref [40] |

Table 2.1: Types of half-metals

The most direct method is spin-resolved photoemission. Emitted electrons from the materials can be detected by the Mott electron detector [27]. From the spin resolved measurement one can directly obtain the spin polarization of the material at the Fermi surface. The spin polarization of Perovskites manganite La_{0.7}Sr_{0.3}MnO₃ was measured as $100\pm 5\%$ at the Fermi surface using spin-resolved photoemission by J. H. Park and collaborators [34].

Photoemission, however, is a technology that largely depends on the surface conditions of the samples. The possible change of the stoichiometry at the surface and the defects at the surface might affect the experimental results. There has been evidence, however, showing that the half-metallic properties are preserved at the surface for some materials [44]. Another disadvantage of spin-resolved photoemission, besides

the surface sensitivity, is that it requires ultra-high vacuum conditions and careful preparation of samples. It is not a technique which can be easily applied to check a large number of samples for half-metallic behavior.

Another important experimental method of spin polarization measurement is Point Contact Andreev Reflection (PCAR). Figure 2.1 shows a diagram of how the PCAR measurement works.

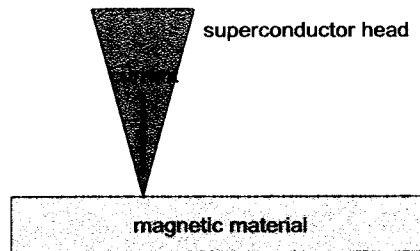


Figure 2.1: Point contact Andreev reflection

The superconductor head and the material to be measured have a direct mechanical contact. A current goes through the junction. If the material is half-metallic, the electrons going into the superconductor will be blocked and reflected because the half-metal doesn't offer minority electrons to form Cooper pairs with the majority electrons. If the material is not half-metallic, spin polarization can also be measured, because it affects the current also. Only when the material has a zero spin polarization does it not affect the current. Table 2.2 shows the measured spin polarizations of many important magnetic materials using PCAR by R. J. Soulen et.al. [45, 46]. From the table one can see CrO_2 has the highest measured spin polarization value (90%) among all the materials. In 2001, a PCAR experiment on an epitaxially grown

single crystal CrO₂ film showed a spin polarization of 96±1% [3].

| samples | NiFe | Co | Ni | Fe | NiMnSb | LSMO | CrO ₂ |
|----------------------------|------|-----|-----|-----|--------|------|------------------|
| measured spin polarization | 40% | 40% | 40% | 40% | 50% | 80% | 90% |

Table 2.2: Measured spin polarizations of some materials using PCAR

PCAR is a powerful and accurate experimental method. But it needs low temperature conditions, and it's hard to carry out. Even worse, it can't be applied to some materials, e.g. magnetite. Fe₃O₄ undergoes a phase transition known as Verwey transition at 120 K, below which the material is insulating [47]. Any superconducting methods, including PCAR, are not able to measure its spin polarization even it is predicted to be a half-metal at low temperature [30].

Magnetic tunnel junction (MTJ) is a method to measure spin polarizations that doesn't rely on the temperature. The idea of MTJ was presented in Chapter 1. One needs to measure the MR of the magnetic tunnel junction and deduce the spin polarization of the magnetic material inversely. The relation between the MR and the spin polarization P can be obtained from Julliere's formula, introduced in Chapter 1 [6]:

$$MR = \frac{2P^2}{1 - P^2} \quad (2.1)$$

A disadvantage of MTJ is that one has to make a device in order to measure the spin polarization. Another disadvantage is that the measured results rely on the interface conditions and the selection of the barrier materials.

Table 2.3 is a list of the experimental methods in spin polarization measurements. It should be noted, however, none of these methods is perfect for checking if a material is half-metallic. This is because the half-metallic behaviors are actually very

| methods | pros | cons |
|--------------------------|---|--|
| spin resolve PEM | non-destructive, wide temperature range, the most direct method | too sensitive to the surface conditions |
| magnetic tunnel junction | wide temperature range | results depend on the choice of the barrier layer |
| point contact (or PCAR) | accurate | conducted only at low temperature, non-universal (doesn't work for some materials) |

Table 2.3: experimental methods of spin polarization measuring

complicated. Some people even questioned the existence of half-metallic materials by considering their structural defects and the finite temperature effects [48]. Nevertheless, half-metals are a new “playground” of material science due to their broad applications. For now, there are many people working in this area. Some people are even working on the theoretical search of half-metallic ferrimagnetic materials and half-metallic anti-ferromagnetic materials despite of the seemingly impossibility [49, 50].

2.2 CrO₂

2.2.1 Introduction

Chromium Dioxide (CrO₂), as mentioned, has long been used as a tape recording medium. But only until recent discovery of its half-metallic properties did it begin to attract much attention from researchers [1]. Being one of the half-metals with very simple crystal structure and relatively high Curie temperature, CrO₂ has been considered a promising candidate for spintronic devices and spin-injectors. There have been many experiments conducted to explore the applications of CrO₂. In 1990,

vacuum tunnelling of the spin polarized electrons from CrO_2 to Cr single crystal was observed [51]. In addition, high frequency impedance spectra were studied to explore its high frequency device applications [52], and large inverse MR was observed recently by J. S. Parker et al. in CrO_2/Co junctions with an artificial barrier [53].

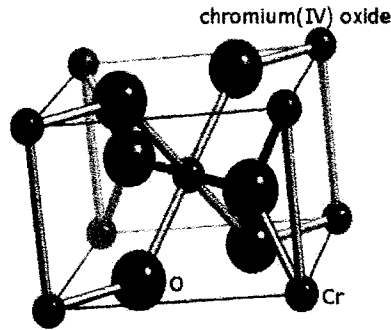


Figure 2.2: Crystal structure of CrO_2

Half metallic CrO_2 is a transition metal oxide with rutile structure and lattice constants of $a=b=4.421 \text{ \AA}$ and $c=2.916 \text{ \AA}$. Its basic structure is shown in Figure 2.2. Surprising for an oxide, it is a ferromagnetic metal below the Curie temperature (386 K). The magnetic easy axis is along (001) direction (corresponding to the c -axis). The Cr^{4+} ion has a complete Ar shell plus two 3d electrons. Correspondingly, each O^{2-} ion in the crystal has a He shell plus six 2p electrons. At the oxygen sites, the crystal field leads to two sp^2 combinations formed by the 2s and $2p_x$, $2p_z$ electrons, and a $2p_y$ state whose orbital plane is perpendicular to c -axis. For the chromium sites, the crystal field splits the 3d bands into three t_{2g} states and two e_g states. In the local coordinate system, the 3 t_{2g} orbitals can be expressed as the natural base $3d_{xy}$, $3d_{xz-yz}$ and $3d_{xz+yz}$. One of the t_{2g} states, namely $3d_{yz-xz}$, is hybridized with the

oxygen $2p_y$ state and forms a π -type state near the Fermi level [23, 54]. The strong orbital anisotropy has been previously investigated with optical spectroscopy [55] and polarization-dependent x-ray absorption spectroscopy [54].

2.2.2 Theoretical Bandstructure Calculations

CrO_2 was first predicted as a half-metallic ferromagnet in 1986 by K. Schwartz [1]. Since then, band structure calculations have been performed using different approximations [22, 23, 24, 56]. Table 2.4 is a list of the research groups who performed band structure calculations and the approximation methods they used [57, 58, 59].

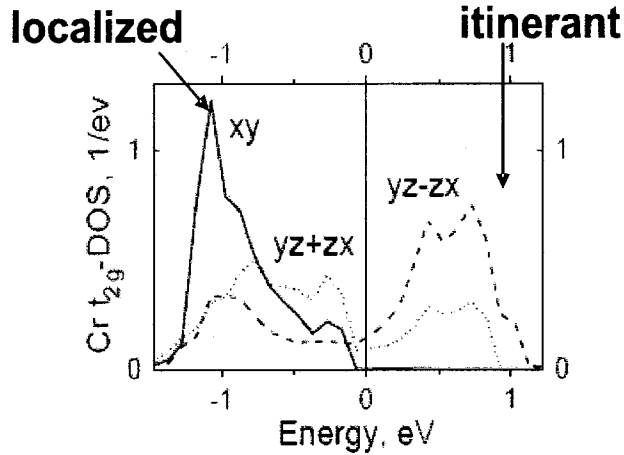


Figure 2.3: Partial Cr t_{2g} majority spin density of states in the vicinity of the Fermi level [23]

Among all these research groups, M. A. Korotin et al. were the first to attribute the ferromagnetism of CrO_2 to the double exchange mechanism of the material. The concept of double exchange mechanism of CrO_2 was later explained in detail by P.

Schlottmann [60]: One of the two 3d electrons occupies the $3d_{xy}$ state, which is localized and forms a spin up “core”. Another 3d electron partly fills the Cr $3d_{yz+xz}$ band and the hybridization band of the O $2p_y$ and Cr $3d_{yz-xz}$, and is itinerant. It propagates through the spin up “cores” and aligns its spin with them resulting in a double exchange mechanism. These band structure calculations are mostly based on the local-spin-density approximation (LSDA). All of them agree that CrO_2 is half-metallic. The controversy, however, is how important the electron correlation is. While some of them think the electron correlation should be considered, which leads to LSDA+U calculation [23], some others think LSDA calculation results are reconcilable with the experimental data [59]. A Raman mode was predicted by S. P. Lewis et al. according to the theoretical calculation and was later confirmed by M. N. Iliev and collaborators’ experimental work [61].

| report year | researcher/researchers | methods |
|-------------|--------------------------------|---|
| 1986 | K. Schwarz, Ref [1] | LSDA, ASW (augmented spherical wave) |
| 1997 | S. P. Lewis et al., Ref [22] | LSDA, PWPP (plane-wave pseudopotential) |
| 1998 | M. A. Korotin et al., Ref [23] | LSDA+U, LMTO (linearized muffin-tin orbitals) |
| 1999 | I. I. Mazin et al., Ref [24] | LSDA, LAPW (linearized augmented plane-wave), GGA (generalized gradient approximation) |
| 2000 | N. E. Brener et al., Ref [57] | LSDA, full potential LCGO (linear combination of Gaussian orbitals) |
| 2003 | L. Craco et al., Ref [58] | LSDA+DMFT (dynamical mean field theory) |
| 2004 | A. Toropova et al., Ref [59] | LSDA and LSDA+U |

LSDA:local spin density approximation

Table 2.4: Theoretical calculation of CrO_2 band structure

Besides these band structure calculations, many theoretical calculations were performed on the magneto-optical properties of the material. In many half-metals, e.g. NiMnSb, it was suggested magneto-optical effect is more or less related with the spin

polarization [62]. But for CrO_2 , these calculations ended in small Kerr angles [63, 64]. The largest Kerr angle of CrO_2 exists at 3.7 eV, where the rotation is 0.154° , although it was found at the low temperature that the magneto-optical effect is significantly enhanced over that at the room temperature [65].

2.2.3 Spin Resolved Photo Emission and PCAR

Spin resolved photo emission is the most direct method for measuring spin polarization. Unfortunately, the photo emission experiment is very sensitive to the surface condition. Although according to the electronic structure calculation H. van Leuken and R. A. de Groot concluded the half-metallic character of CrO_2 is maintained up to the surface [66], in reality the surface of the CrO_2 film is often covered by a thin layer of Cr_2O_3 due to the surface decomposition. In 1987 K. P. Kämper et al. reported on spin resolved photo emission study of CrO_2 polycrystalline film [2]. An ion beam was used to first clean the surface of the film. Nearly 100% spin polarization was found for 2 eV below the Fermi level, but at the Fermi surface the sample seemed to be insulating for both majority and minority electrons. In 1999, high quality epitaxial single crystal CrO_2 films were reported to be obtained by chemical vapor deposition (CVD) [67]. The growth of the same samples by liquid precursor was also made possible soon [68]. The development of the sample fabrication technology offered many opportunities to study high quality epitaxial films. In 2002, Yu. S. Dedkov et al. performed spin resolved photo emission study on single crystal CrO_2 film and found a spin polarization of up to 95% at the Fermi surface at room temperature [27]. An-

other experimental proof of half-metallic character of CrO₂ was from PCAR, the spin polarization was measured to be 96±1% by Y. Ji and his coworkers [3]. For now, it seems there's no doubt the CrO₂ is half-metallic.

2.2.4 Critical Behavior

Although the critical-point indices studies for CrO₂ had been reported in 1967 [69], an accurate measurement of the indices of the single crystal epitaxial film wasn't reported until 2001 [70]. According to these indices, epitaxial CrO₂ films were found to be a 3d Heisenberg ferromagnet. The Curie temperature was reported as 386.50±0.05K, which might be the most accurate measurement of CrO₂'s Curie temperature so far.

2.2.5 Transport Measurements

Temperature dependent transport properties were explored on compressed powder samples [71, 72, 5]. The resistivity was found to comply with the phenomenological expression:

$$\rho = \rho_0 + \alpha T^2 e^{-\Delta/T} \quad (2.2)$$

The cut-off temperature Δ was considered as the point below which the spin flip scattering processes are suppressed, because in a half-metallic material, there are no available final states. Above this temperature, however, the resistivity follows T² law; and at the room temperature, the material becomes a “bad metal”, with a large resistivity exceeding the Ioffe-Regal limit.

A considerably large MR was also discovered for polycrystalline CrO_2 films. The MR was proven to be extrinsic [25, 26]. It was experimentally illustrated the Cr_2O_3 barrier on the CrO_2 grains plays an important role in the spin tunneling processes, and hence contributes to the MR effect.

2.2.6 Optical Spectroscopy Study

Optical spectra studies are very closely related with the transport studies. The earliest optical spectra study of CrO_2 goes back to 1974, when L. L. Chase obtained polarization dependent absorption spectroscopy of CrO_2 deposited on TiO_2 substrate by high pressure decomposition process [55]. Absorption edge of 1.5 eV was observed together with other three absorption peaks at 2 eV, 2.7 eV and 3.1 eV. There were no band structure calculations available at the time, and the results were explained qualitatively. In 1999, an infrared spectroscopy obtained by E. J. Singley et al. showed that the optical conductivity of CrO_2 is very high at low frequencies [4]. This is also explained by the lack of spin-flip scattering processes. Figure 2.4 is a cartoon of spin resolved density of states (DOS) of CrO_2 , which explains why there is a frequency offset.

R. Yamamoto et al. exploited the double exchange mechanism to explain their temperature dependent absorption spectroscopy. Thus the magnetic properties are related with the optical properties of the CrO_2 . The on-site Hund's coupling and the energy splitting between the localized and itinerant state were found to be 0.5 eV and 1 eV respectively [73].

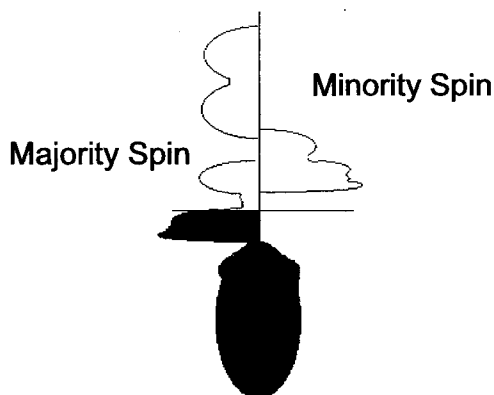


Figure 2.4: A cartoon of spin resolved DOS of CrO_2

2.2.7 Orbital Moments

The earliest experimental investigation of oxygen orbitals in CrO_2 was reported in 2000, where polarization dependent x-ray absorption spectroscopy (XAS) was used [54]. The O $2p_y$ states were found to be hybridized with Cr $3d_{xz-yz}$ t_{2g} states. The hybridized states form a π -type band with a band width of about 0.7 eV. The exchange splitting energy was found to be about 3 eV, and correlation effects were also confirmed. In 2001, Mukul S. Laad et al. Developed a model for the description of CrO_2 [74], in which they believed correlation effects were important to understand the metallic phase of CrO_2 . D. J. Huang et al. also found the on-site Coulomb energy is essential to describe the orbital magnetic moments of the material [75]. The anisotropy of the orbital moments in CrO_2 was observed and studied by x-ray magnetic circular dichroism (XMCD) [76]. The theoretical calculation revealed the orbital anisotropy is actually a factor of five smaller than what the XMCD experiments suggested, but still much bigger than Fe, Co and Ni [77]. Both XAS and

XES (x-ray emission spectroscopy) experiments have shown evidence of half-metallic behavior [78, 79].

2.2.8 Magnetic Measurements

Vibrating sample magnetometry (VSM) was used to measure the hysteresis curves of epitaxially grown CrO₂ [80]. The results show a perfect fit to the coherent rotation model. The anisotropy energy term was:

$$E = k_0 + k_1 \sin^2 \theta + k_2 \sin^4 \theta \quad (2.3)$$

where θ is the angle between the magnetic moment and the easy axis. The anisotropy constants were determined as $k_0=1.5 \times 10^4$ erg/cm³, $k_1=2.7 \times 10^5$ erg/cm³ and $k_2=7.5 \times 10^4$ erg/cm³. This coherent rotation model was used to explain the time resolved MOKE (TRMOKE) data taken by Nurmikko's group [12]. In the TRMOKE experiments, oscillations were found when the external field was applied along the hard axis. A careful manipulation of the laser pulses clearly demonstrated how the magnetic moment processes. One thing not clear about the TRMOKE results was the easy axis data. Oscillations could be found for many other materials even when the applied field is a few degrees off the easy axis. But for CrO₂, the oscillations were very hard to detect if the angle between the easy axis and the applied field is smaller than 45°. This confusion could seem to be explained by the switching mechanism of magnetic moment. I. L. Siu et al. reported their high resolution interference-contrast-colloid (ICC) data, which show the switching mechanism of the

magnetic moment along the easy axis is dominated by the motion of domain wall and the switching along the hard axis is dominated by the coherent rotation [81]. The uniaxial anisotropy is not the only anisotropy energy term. Both the temperature dependent hysteresis curves measurements [82] and the temperature dependent magnetic susceptibility measurements [83] have shown the strain effect to be very important to understand the anisotropy of CrO_2 . Under certain conditions, the strain effect could dominate, especially for the thin samples at low temperature, in which case the magnetic easy axis could switch from c-axis to b-axis. The magneto transport properties have shown substrate dependence, which also implies the importance of the strain effect [84]. Ferromagnetic resonance (FMR) is an independent way to study the anisotropies of CrO_2 [85]. Strain effects have also been observed in FMR studies [86].

Chapter 3

Theory of Ultrafast Laser Pump-Probe Spectroscopy and MOKE

This chapter discusses the basic theories behind the experimental procedures used in this thesis work. The goal of this thesis work was to apply the ultrafast laser pump-probe technique, which has been so successful in the study of a wide variety of materials, to the half-metallic CrO_2 . Furthermore, the magneto-optical Kerr effect was used to learn about the static and dynamic magnetization of CrO_2 . This chapter will give an overview of the concepts behind the ultrafast pump-probe procedure and MOKE.

3.1 Ultrafast pump-probe spectroscopy

The principle of ultrafast pump-probe experiments is quite straightforward. In these experiments, lasers which output pulses with very short duration are used (lasting on the order of femtoseconds or picoseconds). The laser beam is split into two paths: a pump and a probe. The sample to be studied is first hit by a pump pulse, and an excited state is created (e.g., carriers are excited to the conduction band in a semiconductor). A probe pulse, delayed in time by sending it through a longer path

by use of a motion stage, hits the sample and is reflected by or transmitted through the sample. A basic schematic of the pump-probe experiment is shown in Figure 3.1. The information of the excited states of the sample is brought out by measuring the reflected or transmitted probe pulse. The pump-probe experiment is a typical method used for studying materials in their excited states and provides a direct way of measuring the lifetime of many types of excitations [14]. The pump-probe technique has been used with great success to study a wide variety of materials, from semiconductors to biological molecules.

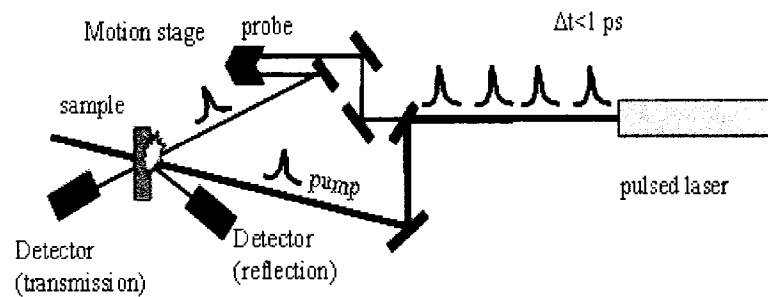


Figure 3.1: Pump-probe experiment setup

Pump-probe experiments can be done in different wavelength ranges, and the pump and probe don't have to have the same wavelength. Actually, two-color pump-probe experiments have proved to be a powerful tool in study of the band structure of semiconductors, as well as strongly correlated systems [87, 88].

In pump-probe experiments, the pump pulses and the probe pulses have to be synchronized. An ultrafast photodetector is not required because the time delay between the pump pulse and the probe pulse is controlled by a motion stage, and

measuring the probe pulses is like taking a “snapshot” of the material while it is in an excited state. This is another advantage of pump-probe experiments.

The intensity ratio of the probe and the pump should be kept small to avoid any self-excitation by the probe beam. Furthermore, in many material studies, for example, in the pump-probe studies of high temperature superconductors [89], both the pump and the probe should be kept weak, so the material can be raised to an excited state but the properties of the materials won't be permanently altered. In these cases, the pump-probe experiment is considered a perturbation method.

The ultrafast pump-probe laser technique involves nonlinear effects, since the pump laser pulses are strong enough to momentarily modify the electronic and optical properties of materials. The interaction of the light with materials can be described through the optical polarization, \mathcal{P} :

$$\vec{\mathcal{P}} = \epsilon_0(\chi^{(1)}\vec{E} + \chi^{(2)}\vec{E} \cdot \vec{E} + \chi^{(3)}\vec{E} \cdot \vec{E} \cdot \vec{E} + \dots) \quad (3.1)$$

where $\chi^{(n)}$ is the n-th order susceptibility and \vec{E} is the optical electric field. The first order term describes linear absorption and reflection processes, where the light does not perturb the material system. The higher order terms, which are nonlinear in E , describe processes where the light does modify the material system, as the pump does in the pump-probe experiment. To theoretically describe the nonlinear effects, one would start with the polarization, since the polarization gives rise to a resulting electric field which is emitted from the sample and detected.

In the pump-probe experiment, the polarization is probed either through reflection

or transmission. In transmission, the intensity of the probe beam on a detector is measured, and can be described by Beer's Law according to the absorption coefficient, α :

$$I_{DT} = I_{on} - I_{off} = I_0 \exp(-(\alpha - \Delta\alpha)L) - I_0 \exp(-\alpha L) \quad (3.2)$$

Where L is the thickness of the sample and I_{on} and I_{off} would be the intensity measured by the photodetector if the pump beam were present or absent, respectively. This is done in practice by sending the pump laser beam through an optical chopper which momentarily blocks the beam at a regular rate. Above, $\Delta\alpha$ describes the change in absorption brought about by application of the pump pulses. It is proportional to the nonlinear polarization described above.

Metals and semiconductors show different behaviors in pump-probe experiments due to their different electronic structure. In the pump-probe studies of semiconductors, band structure plays an important role in understanding the experimental results [88]. The ultrafast spectroscopy is generally wavelength dependent. This is understandable because the ultrafast spectroscopy of semiconductors illustrates the transition of the electrons from band to band (e.g., valence to conduction), as well as the intra-band scattering. The pump-probe curves of semiconductors normally have many decay components, corresponding to electron-electron scattering, inter-band transition, electron-phonon scattering, etc.. Nonlinear experiments such as the pump-probe technique in semiconductors are frequently described theoretically using atomic-like level models to represent the different states. A density matrix formalism [90] is used to calculate the nonlinear polarization and the behavior of the

resulting signals.

The pump-probe experimental results of metals, although different for each individual metal, are generally simpler [91]. The pump pulses excite electrons at the Fermi surface. The main decay mechanism is the recovering of the electrons to the Fermi surface and the releasing of their heat to the lattice. A classical theory of the ultrafast spectroscopy of metals is called two-temperature model, where the electrons and the phonons are considered in two separate reservoirs, each having its own temperature. The pump pulse injects energy into the electron reservoir and the probe pulse detects the activity of the electrons during the energy exchange process between the two reservoirs. Note that this model assumes that the pump-probe delay times are much greater than the electron thermalization time.

The two temperature model can be described by the following equations:

$$C_e(T_e)\frac{\partial T_e}{\partial t} = \frac{\partial}{\partial z} \left(K_e \frac{\partial T_e}{\partial z} \right) - g_{el}(T_e - T_l) + S(z, t) \quad (3.3)$$

$$C_l(T_l)\frac{\partial T_l}{\partial t} = g_{el}(T_e - T_l) \quad (3.4)$$

Where

$$S(z, t) = (1 - R)I_0\alpha e^{-\alpha|z|}e^{-(t/\tau)^2} \quad (3.5)$$

is the source term, representing the impact of the pump pulses. Here, α is the absorption coefficient and R is the reflectivity, K_e is the thermal conductivity and g_{el} represents the electron-lattice (phonon) coupling. C_e and C_l represent the heat capacity of the electron reservoir and the phonon reservoir respectively. Using these

equations, the temperature of the electrons and lattice can be calculated as a function of time. The temperature directly affects the absorption and reflectivity of the material, which is probed in the experiment. For ferromagnetic metals, the spin system can also be included by adding another equation above for the spin system (the three temperature model):

$$C_s(T_s)\frac{\partial T_s}{\partial t} = g_{es}(T_e - T_s) + g_{sl}(T_l - T_s) \quad (3.6)$$

as well as modifying the electron and lattice equations:

$$C_e(T_e)\frac{\partial T_e}{\partial t} = \frac{\partial}{\partial z} \left(K_e \frac{\partial T_e}{\partial z} \right) - g_{el}(T_e - T_l) - g_{es}(T_e - T_s) + S(z, t) \quad (3.7)$$

$$C_l(T_l)\frac{\partial T_l}{\partial t} = g_{el}(T_e - T_l) - g_{sl}(T_s - T_l) \quad (3.8)$$

As an example, in Figure 3.2, the pump-probe transmission from Ni measured by Beaurepaire et al. is shown. The contributions of the three temperature reservoirs: electron, lattice and spin, are also shown [15].

Half-metallic materials such as CrO_2 are an interesting case to study by nonlinear spectroscopy. CrO_2 is a metal, so we expect that their behavior will be mostly described by the two or three temperature model. However, we expect wavelength-dependent features in the visible range which indicate its unique bandstructure.

3.2 Magneto-optical Kerr Effect (MOKE)

When a beam of linearly polarized light is reflected by a ferromagnetic material, the polarization of the reflected light will experience a change in angle of orientation as

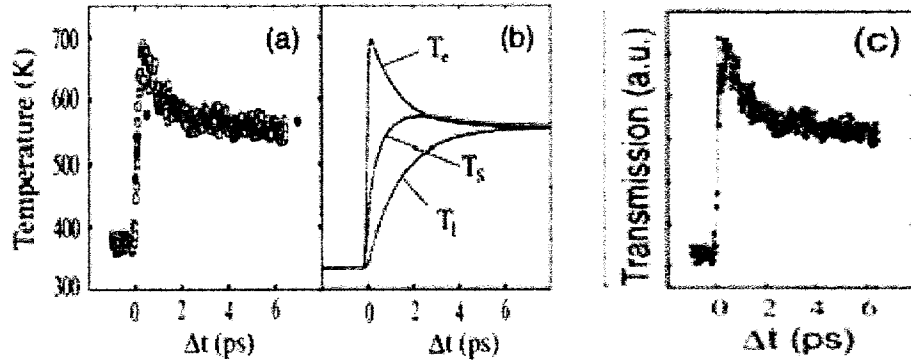


Figure 3.2: From ref [15] (a) Estimated temperature taken from pump-probe transmission signal from Ni (c), along with calculations based on the three temperature model (b). The temperature scale was determined by measuring the pump-induced decrease in the saturation magnetization.

well as in ellipticity. The magnitude of the polarization rotation (Kerr rotation) and the ellipticity change (Kerr ellipticity) are different for different materials. Both the Kerr rotation and ellipticity are proportional to the magnetization, and can be used to probe the magnetization of ferromagnetic thin films.

There are three configurations to observe MOKE experimentally. They are described as longitudinal MOKE, polar MOKE and transverse MOKE.

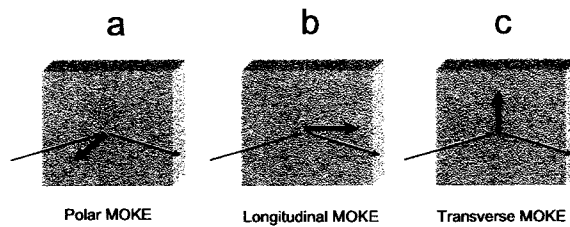


Figure 3.3: (a) Polar MOKE, (b) Longitudinal MOKE, and (c) Transverse MOKE

In the polar configuration (Figure 3.3a), the magnetization of the material points

perpendicular to the surface of the material. Both Kerr rotation and Kerr ellipticity are observed in this case, and they are proportional to the magnitude of the magnetization.

In the longitudinal configuration (Figure 3.3b), the magnetization of the material lies in the incident plane of the light beam. Both Kerr rotation and Kerr ellipticity are observed in this configuration, and they are proportional to the magnitude of the magnetization.

The transverse configuration (Figure 3.3c) is a little more complicated. There's no Kerr rotation or Kerr ellipticity observed in this configuration. However, the reflectivity changes with the magnetization of the material, and the change is proportional to the magnitude of the magnetization.

The MOKE, fundamentally, is due to the asymmetry of the materials absorption for Left Circularly Polarized (LCP) light and Right Circularly Polarized (RCP) light [92, 93], due to bandstructure and spin-orbit coupling.

Consider a cubic lattice for simplicity, the conductivity of the solid can be written as:

$$\sigma(\omega) = \begin{pmatrix} \sigma_{xx} & \sigma_{xy} & 0 \\ -\sigma_{xy} & \sigma_{xx} & 0 \\ 0 & 0 & \sigma_{xx} \end{pmatrix} \quad (3.9)$$

Each of the above matrix elements can be a complex number and be further written as $\sigma_{ij} = \sigma_{1ij} + i\sigma_{2ij}$, in which the diagonal term σ_{2xy} is proportional to the difference in absorption of LCP and RCP light. It can be written as [94, 93]:

$$\sigma_{2xy}(\omega) = \frac{e^2}{2m^2\hbar} \sum_{if} \left(\frac{|\pi_{if}^-|^2}{(\omega_{if}^-)^2 - \omega^2} - \frac{|\pi_{if}^+|^2}{(\omega_{if}^+)^2 - \omega^2} \right) \quad (3.10)$$

In which π^\pm and ω^\pm are the momentum operator and the energy operator for RCP and LCP respectively, and i and f represent the initial state and the final state for the optical transition. The momentum operator has the form:

$$\pi = p + (e/c)A + (1/2mc^2)\sigma \times \nabla \quad (3.11)$$

Where p is the electron momentum, A is the vector potential describing the electromagnetic radiation and σ is the spin operator (the last term above describes the spin-orbit interaction). For magnetic materials, the LCP term and the RCP term of Equation 3.10 may not be canceled in general, giving rise to the off-diagonal terms in the conductivity. The dielectric tensor, from which arise the absorption and reflectivity coefficients, is directly proportional to the conductivity.

$$\epsilon_{ij} = 1 + i4\pi\sigma_{ij}/\omega \quad (3.12)$$

If the direction of the magnetization has an Euler's angles (m_x, m_y, m_z), the dielectric tensor of the material can be written as [95, 96]:

$$\epsilon = \epsilon_{xx} \begin{pmatrix} 1 & -iQm_z & iQm_y \\ iQm_z & 1 & -iQm_x \\ -iQm_y & iQm_x & 1 \end{pmatrix} \quad (3.13)$$

Where $Q=i\epsilon_{xy}/\epsilon_{xx}$ is defined as magneto optical constant. And, the Fresnel reflection matrix can be written as:

$$\mathfrak{R} = \begin{pmatrix} r_{pp} & r_{ps} \\ r_{sp} & r_{ss} \end{pmatrix} \quad (3.14)$$

Where r_{ij} is the ratio of the incident j polarized electric field and the reflected i polarized electric field. Solving Maxwell's equations for the electric tensor in Equation 3.13, the elements of Fresnel reflection matrix can be written as:

$$r_{pp} = \frac{n_1 \cos \theta_0 - n_0 \cos \theta_1}{n_1 \cos \theta_0 + n_0 \cos \theta_1} - \frac{i 2 n_0 n_1 \cos \theta_0 \sin \theta_1 m_x Q}{n_1 \cos \theta_0 + n_0 \cos \theta_1} \quad (3.15)$$

$$r_{sp} = \frac{i n_0 n_1 \cos \theta_0 (m_y \sin \theta_1 + m_z \cos \theta_1) Q}{(n_1 \cos \theta_0 + n_0 \cos \theta_1)(n_0 \cos \theta_0 + n_1 \cos \theta_1) \cos \theta_1} \quad (3.16)$$

$$r_{ss} = \frac{n_0 \cos \theta_0 - n_1 \cos \theta_1}{n_0 \cos \theta_0 + n_1 \cos \theta_1} \quad (3.17)$$

$$r_{ps} = -\frac{i n_0 n_1 \cos \theta_0 (m_y \sin \theta_1 - m_z \cos \theta_1) Q}{(n_1 \cos \theta_0 + n_0 \cos \theta_1)(n_0 \cos \theta_0 + n_1 \cos \theta_1) \cos \theta_1} \quad (3.18)$$

In which θ_0 , n_0 , θ_1 and n_1 are the incident/refractive angles and the indices of refraction for medium0 and medium1, respectively (assume the laser beam goes from medium0 to medium1).

For CrO_2 , the Kerr ellipticity is small in our wavelength range [65]. What we have detected is mainly the signal from Kerr rotation. And, in our experiments, we measure longitudinal MOKE for p-polarized light, where $m_y=1$ and $m_x=m_z=0$, and the Kerr rotation can be written as:

$$\theta = \frac{r_{sp}}{r_{pp}} = \frac{\cos \theta_0 \tan \theta_1}{\cos(\theta_0 + \theta_1)} \cdot \frac{i n_0 n_1 Q}{(n_1^2 - n_0^2)} \quad (3.19)$$

In general, it is very difficult, if not impossible, to write a quantitative relationship between the magnetization and the Kerr ellipticity and rotation. Therefore, it is difficult to use MOKE to measure the magnetization in absolute units. It has been shown, however, to give accurate measurements of the shape of hysteresis loops and hence

the magnetic coercivity (widths) and remanence (relative amount of magnetization at zero applied field).

3.3 Incoherent and Coherent Magnetization Dynamics

When a ferromagnetic system is perturbed, the magnetization can assume different directions by different mechanisms. The two main mechanisms are coherent rotation, where local spins rotate as a whole group, and domain wall motion, where local spin flips occur and propagate through the material.

The coherent rotation model, also known as Stoner-Wohlfarth model, describes the motion of the magnetic moment in which all the spins rotate coherently while they are under the influence of the external magnetic field. In coherent rotation model, the coercivity is mainly determined by the anisotropy of the material. If we only consider the simplest uniaxial anisotropy term, the potential energy of the system can be written as

$$U = -MH\cos(\phi - \theta) - K\sin^2\theta \quad (3.20)$$

Where ϕ and θ represent the angle between the external fields and the hard axis, and the angle between the magnetic moment and the hard axis respectively. For any given external field H , one can always find the equilibrium angle θ by minimizing the total potential energy. From this, the instantaneous direction of the magnetization, and thus the hysteresis loop, can be obtained.

Most macroscopic thin films contain magnetic domains, or local regions of magnetic order. If a domain is too large, it will break into smaller pieces to reduce the potential energy caused by the higher order terms, for example, the self demagnetization effect. Domain walls are created between areas of local order. Application of an external magnetic field can cause the growth of domains that are along the field direction and reduce the size of the domains where the spins are against the external field. Thus an applied field causes the motion of domain walls, until the magnetization is finally saturated. This flipping process is much slower than the coherent rotation of the magnetic moment, which usually doesn't take more than 100 ps.

Both of these two flipping processes exist in thin film CrO₂ [81]. If the external field is along the hard axis of the sample, the magnetic moment follows the coherent rotation model; and if the external field is away from the hard axis, the motion of the domain walls is observed.

3.4 Magnetization Dynamics

Current scientific interest is in regards to coherent magnetization processes, since they are very fast and can be useful for fast switching process. For coherent rotation, the motion of the magnetic moment can be well described by Landau-Lifshitz-Gilbert (LLG) equation [97]:

$$\frac{\partial \vec{M}}{\partial t} = -\gamma \vec{M} \times \vec{H} + \frac{\alpha}{M_s} (\vec{M} \times \frac{\partial \vec{M}}{\partial t}) \quad (3.21)$$

Here, γ is the gyromagnetic ratio, \vec{M} is the magnetization. M_s is the magnitude

of the saturation magnetization and α is a damping coefficient. The magnetic field \vec{H} represents not only an externally applied magnetic field, but also any internal fields, such as due to anisotropy, present in the sample. The LLG equation describes the rotation of magnetic moments back to an equilibrium position, after being perturbed from the equilibrium. The $\vec{M} \times \vec{H}$ term is basically a torque term. Figure 3.4 illustrates the relaxation back to equilibrium which the LLG equation describes.

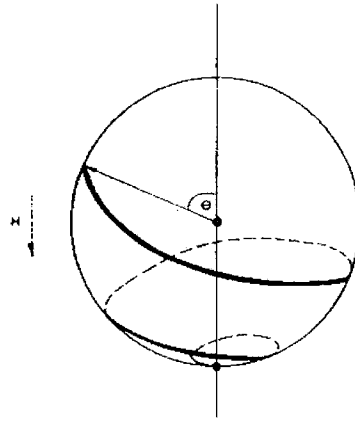


Figure 3.4: The motion of magnetic moment as described by the LLG equation [97]

The LLG is a vector equation. Assuming a simple case where the magnetic field \vec{H} is applied in the z -direction, components of the LLG equation can be written as [97]:

$$\frac{\partial M_x}{\partial t} = \frac{\omega_0}{1 + \alpha^2} M_y + \frac{\omega_0 \alpha}{1 + \alpha^2} \frac{M_x M_z}{M_s} \quad (3.22)$$

$$\frac{\partial M_y}{\partial t} = -\frac{\omega_0}{1 + \alpha^2} M_x + \frac{\omega_0 \alpha}{1 + \alpha^2} \frac{M_y M_z}{M_s} \quad (3.23)$$

$$\frac{\partial M_z}{\partial t} = -\frac{\omega_0 \alpha}{1 + \alpha^2} M_s + \frac{\omega_0}{1 + \alpha^2} \frac{M_z^2}{M_s} \quad (3.24)$$

Where $\omega_0=\gamma H$ is the Larmor frequency in the non-damping case. This is a three dimensional nonlinear differential equation. The solution for it is:

$$M_x = M_s \sin\theta e^{i\omega t} \quad (3.25)$$

$$M_y = M_s \sin\theta e^{i(\omega t + \pi/2)} \quad (3.26)$$

$$M_z = M_s \cos\theta \quad (3.27)$$

Where $\tan(\theta/2) = e^{t/\tau+c}$, $\omega = \frac{\omega_0}{1+\alpha^2}$, $\tau = \frac{1+\alpha^2}{\omega_0\alpha}$, and c is a constant determined by the initial conditions. If we choose c=0 as our initial condition, then we have:

$$\tan\frac{\theta}{2} = e^{t/\tau} \quad (3.28)$$

$$\sin\theta = \frac{2e^{t/\tau}}{1 + e^{2t/\tau}} \quad (3.29)$$

$$\cos\theta = \frac{1 - e^{2t/\tau}}{1 + e^{2t/\tau}} = \tanh\frac{t}{\tau} \quad (3.30)$$

And the solution of the LLG equation can be written as:

$$M_x = M_s \frac{2e^{t/\tau}}{1 + e^{2t/\tau}} \sin\omega t \quad (3.31)$$

$$M_z = M_s \tanh\frac{t}{\tau} \quad (3.32)$$

The above solutions illustrate sinusoidal time dependence, or oscillations. Thus, we expect to observe the oscillations in our longitudinal ultrafast MOKE experiments.

The above analysis illustrates the general behavior of the magnetization dynamics described by the LLG equation. Magnetization dynamics in CrO₂ are discussed in

Chapter 7, where the LLG will be used to describe the magnetization oscillations which occur after a pump-induced decrease in magnetic anisotropy. A more rigorous analysis of the LLG is needed in order to extract information about anisotropy from the measured magnetization oscillations.

3.5 FMR Analysis of the LLG

To describe the relationship between the external and internal magnetic fields and the coherent oscillation frequencies, we turn to an analysis commonly used in ferromagnetic resonance (FMR). In this analysis, it is assumed that the magnetization is only slightly perturbed from its equilibrium value.

In ferromagnetic resonance, the oscillation frequency can be written as [98]:

$$\left(\frac{\omega}{\gamma}\right)^2 = \frac{1}{(M \sin \theta)^2} \left(\frac{\partial^2 F}{\partial \theta^2} \frac{\partial^2 F}{\partial \varphi^2} - \left(\frac{\partial^2 F}{\partial \theta \partial \varphi} \right)^2 \right) \quad (3.33)$$

Where γ is the gyromagnetic ratio, M is saturation magnetization, and F is the free energy of the system.

In our system, if we only consider uniaxial anisotropy and stress anisotropy, the free energy can be written as:

$$F(\theta, \varphi) = -HM \cos(\varphi - \varphi_h) \sin \theta + \frac{H_u M}{2} \cos^2 \theta + K_u \sin^2 \varphi + K_\delta \sin^2(\varphi - \delta) \quad (3.34)$$

Where H is the applied field; M is the saturation magnetization; φ is the angle between the in plane magnetic moment and the easy axis; θ is the angle between the

magnetic moment and the normal of the film; φ_h is the angle between the applied field and the easy axis; H_d is the demagnetization field; K_u is the uniaxial anisotropy constant, and K_δ and δ represent the stress anisotropy constants and its direction respectively.

If the external field is applied along the hard axis, then $\varphi_h = \pi/2$ and $\theta = \pi/2$, and the FMR frequency ($f=2\pi\omega$) according to Equation 3.33, can be written as:

$$f = \frac{g\gamma}{4\pi} \sqrt{(H \sin \varphi + H_d)[H \sin \varphi + (H_{K_u} + H_{K_{\delta c}}) \cos 2\varphi + H_{K_{\delta b}} \sin 2\varphi]} \quad (3.35)$$

Where $g \approx 2$ is the Landau factor; $\gamma = 2\mu_B/\hbar$ is the electron gyromagnetic ratio; $H_{K_u} = 2K_u/M$ is the uniaxial anisotropy field; $H_{K_{\delta c}} = (2K_\delta/M)\cos 2\delta$ and $H_{K_{\delta b}} = (2K_\delta/M)\sin 2\delta$ represent stress anisotropy field along the c-axis and b-axis respectively.

Chapter 4

Experimental Methods

This chapter presents the primary experimental methods of study. This thesis explores the use of ultrafast laser pump-probe spectroscopy to learn about the dynamics and properties of half-metallic CrO_2 . This chapter gives the experimental details of the pump-probe experiment, as well as a description of the growth and properties of the CrO_2 thin films used for this work.

4.1 Ultrafast Pump-probe Experiment

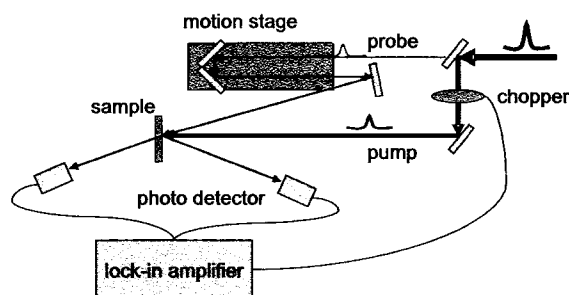


Figure 4.1: Ultrafast pump-probe setup

Since its first applications in chemistry, the ultrafast pump-probe technique has been widely used in scientific research. The essence of the pump-probe technique is

that it takes a “snap shot” of what happens in a very short time period (timescales from femtoseconds to nanoseconds). It is a direct optical method for studying dynamical processes.

An ultrafast pulsed laser system, which outputs pulses of coherent light on the order of 10^{-15} to 10^{-12} seconds, is required for the pump-probe experiment. The basic setup for the pump-probe experiment is shown in Figure 4.1. The ultrafast laser beam, consisting of pulses, is separated by a beam splitter. The part of the beam known as the “pump” is sent to the sample such that it can generate some dynamic process (e.g., excite electronic states in the sample). The other beam, known as the “probe”, is delayed by a certain amount of time by sending it through a longer optical path which can be varied by use of a computer-controlled motion stage. The probe beam is then sent to the sample, and the transmission or reflection of the probe beam from the sample is monitored. By changing the stage position, one can control the time delay between the pump and probe pulses

An optical chopper is placed in the pump beam to add a modulation to the pump beam, and a lock-in amplifier, referencing the same frequency used by the chopper, is used to measure the change of the probe beam incident on a photodetector. The change of the probe beam is solely caused by the pump beam and then must be related with the dynamics of the sample. By controlling the time delay between the pump pulses and the probe pulses and observing the change of the probe pulses, one can study how the sample evolves after being shot by the pump pulses.

An important issue in the pump-probe experiment is the repetition rate of the

pulses. Ideally, it should be as large as possible because larger repetition rate gives higher signal to noise by providing more measurements to the lock-in amplifier during its integration time. However, if the repetition rate is too large, which means the distance between pulses is too short, the sample might not be able to recover from the previous pulse before being shot again, and the average heating effect is unavoidable. In our experiments, we use 1 kHz repetition rate, which is small enough to avoid the average heating.

The laser system used for the thesis work was a Spectra-Physics amplified Titanium Sapphire (Ti:Saph or $\text{Ti:Al}_2\text{O}_3$) all solid state laser system, diagramed in Appendix A. The system starts with a diode-pumped frequency-doubled continuous wave (CW) Nd:YVO₄ laser (Millenia) which is used to pump a modelocked Ti:Saph oscillator (Tsunami). The CW Nd:YVO₄ beam at 532 nm, optically excites transitions within a Ti:Saph crystal in the oscillator laser cavity. The Ti:Saph lases over a wavelength range of 700-1000 nm. The Ti:Saph cavity is actively mode-locked (producing pulsed rather than CW laser action), and produces output pulses of about 150 fs in duration with a repetition rate of 80 MHz.

The oscillator beam seeds a regenerative amplifier cavity (Spitfire), which is essentially another Ti:Saph laser cavity pumped by a diode-pumped frequency-doubled Q-switched Nd:YLF laser (Evolution). The seed laser pulses, if left unaltered with a duration of only 150 fs, would quickly destroy the crystal used for the amplification process. Therefore, the seed pulses are “stretched” to increase their duration by using an optical grating. The stretched pulses are then safely amplified, and then “com-

pressed" back to a duration of 150 fs by means of a grating. The Ti:sapphire amplifier output consists of about 1 mJ, 150 fs duration pulses at 800 nm at a repetition rate of 1 kHz.

The amplified beam pumps a double-pass optical parametric amplifier (OPA) with difference frequency mixer. The OPA works by generating a white light beam, and selecting the light of needed wavelength and amplifying it. The pump beam is split into seed, pre-amp and amp beams. The seed is used to generate a white light beam. The pre-amp beam and amp beam overlap with the seed beam on a Beta Barium Borate (BBO) crystal to amplify it. The BBO crystal is properly oriented for the phase matching condition of the wanted wavelength. The double-pass OPA delivers about 200 μJ , 150 fs duration pulses tunable from 1.1 - 2.7 μm . The wavelength range is extended to 0.2 - 20 μm by difference and sum-frequency mixing producing approximately 2 - 50 μJ , 150 fs pulses over the entire wavelength range.

For the experiments in this thesis, either the amplified Ti:Saph beam or the tunable beam from the OPA was used. As described above, in the pump-probe experiment, the pump beam was optically chopped (Stanford SR540 chopper) and the probe beam was either transmitted through or reflected off of a thin film sample which is placed either in air or in a liquid helium cryostat (Janis) between the poles of an electromagnet or in a magneto-optical liquid helium cryostat (Oxford). The helium cryostats were used to conduct experiments in the temperature ranges of 4 - 300 K. Furthermore, a heater stage in air was used to conduct experiments in the temperature range of 293 - 400 K. The probe beam was detected by a silicon photodiode

(Thorlabs 110). A lock-in amplifier (Stanford Research Systems SR530) was used to detect the effects at the pump beam chopping frequency. For some experiments presented in this thesis, the probe beam reflection from or transmission through the thin films was measured, while for other experiments the Magneto-Optical Kerr effect was monitored. The details of each experiment are given in their respective chapters. An overview of the MOKE experiment is presented next.

4.2 Static Magneto-Optical Kerr Effect (MOKE)

Experiment

The principle of the MOKE effect has been described in the previous chapter. The following picture (Figure 4.2) shows the diagram of the MOKE setup in our lab used to measure static hysteresis loops. In this case, only one CW laser is used.

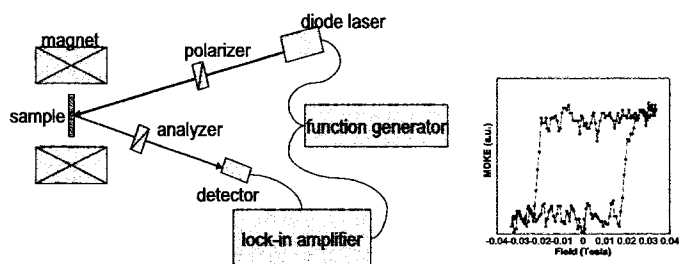


Figure 4.2: MOKE setup and a typical hysteresis loop of CrO₂

A CW polarized diode laser was used for static MOKE. The beam was sent through an extra polarizer to ensure high polarization. The laser beam was reflected from the thin film, which was positioned between the poles of an electromagnet to provide a

varying magnetic field. The reflected beam is sent through a second polarizer, known as the analyzer, which is set to near extinction with the incident laser beam. A function generator is set to modulate the laser diode and trigger the lock-in amplifier, which is used to detect the change of the reflected beam.

If the externally applied magnetic field changes the sample's magnetic moment, the reflected beam polarization will change (both in rotation and ellipticity). This very small change in polarization can be picked up by using the analyzer. Thus the lock-in amplifier reads the polarization change by measuring the intensity change of the reflected beam after the analyzer.

The polarization change of the reflected beam is proportional to the magnetization of the sample. By changing the external magnetic field and measuring the polarization change of the reflected beam, the hysteresis loops of the sample can be measured, although the exact values of the magnetization cannot be measured by MOKE.

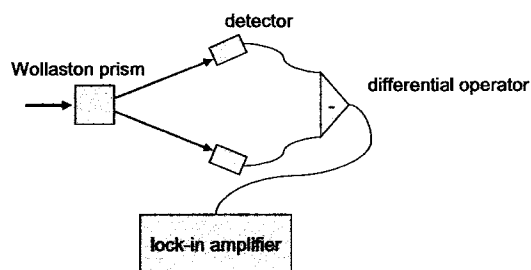


Figure 4.3: Schematic of a balanced detector

We used an analyzer to detect the polarization change. However, a balanced detector instead of an analyzer is more widely used in a typical MOKE system. Figure 4.3 shows a diagram of a balanced detector. A Wollaston prism is used to split

the reflected probe beam, and the two separated beams hit the two photodetectors respectively. At the balanced position, the Wollaston prism is set such that the signals from the two photodetectors cancel with each other, and the net output signal to the lock-in amplifier is zero. If the reflected beam has a polarization change, the net output signal is not zero any more. The output signal is proportional to the magnetization change of the sample.

Ultrafast MOKE experiments can also be done with a pulsed laser system, allowing for measurements of magnetization dynamics. For these experiments, the trigger signal synchronized with the pulse repetition rate is sent to the lock-in amplifier. The pulses can be seen as a modulation.

4.3 Ultrafast MOKE Experiments

Ultrafast MOKE experiments are similar with pump-probe experiments, except the detecting system is adopted from the MOKE setup. Figure 4.4 is a diagram of our ultrafast MOKE setup.

The pulsed laser beam was split as pump and probe. The pump pulses hit the sample and change the magnetization, either by directly decreasing it through electronic and lattice heating, or by affecting anisotropy. The probe pulses were reflected from the sample and sent through an analyzer polarizer and detected by a photodetector which was connected to the lock-in amplifier. Thus the sample's magnetization change caused by the pump can be detected from the polarization change of the probe. Since the delay time between the pump pulses and the probe pulses

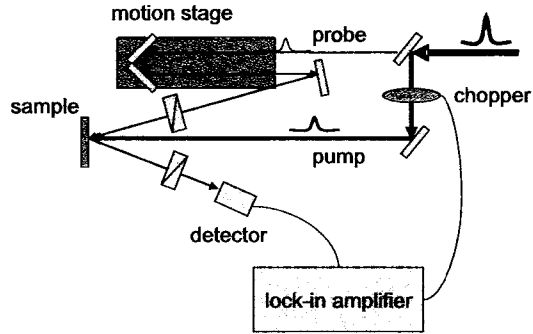


Figure 4.4: Ultrafast MOKE setup

is controlled by a delay stage, the motion of the magnetic moment was studied by adjusting the delay time and observing the magnetization change.

As was discussed previously, the pump beam can either directly modify the magnetization, in which case “snap-shots” of the hysteresis loops and magnetization dynamics can be measured in the time domain. Or, if only magnetic anisotropy is affected and not the magnitude of the magnetic moment, coherent magnetization oscillations are excited, which are detectable through MOKE. Both types of measurements are discussed in the following chapters.

4.4 Sample Preparation and Characterization

Two types of CrO_2 thin films were used in this study. The first group of samples were grown by Dr. Egelhoff’s group at National Institute of Standard Technology (NIST) using high pressure thermal decomposition process [81]. The high pressure method differs from the usual Chemical Vapor Deposition (CVD) method, which is

more popular in CrO_2 single crystal thin film preparation [99]. In CVD method, the temperature and the oxygen flow are fixed at $260\text{ }^\circ\text{C}$ and 100 cc/min respectively. In high pressure method, however, the CrO_3 precursor is heated up to $430\text{ }^\circ\text{C}$ under high oxygen pressure up to $1.4 \times 10^6\text{ Pa}$, and is held for 30 minutes before being quickly quenched back to the room temperature. The CrO_3 decomposes into CrO_2 and is deposited to the single crystal TiO_2 substrates, along the (110) or (100) orientation, depending on the orientation of the substrates. The TiO_2 substrates were polished for the transmission experiments.

The thickness of the films is from a few to several hundred nanometers. The films were characterized with x-ray diffraction experiments and were found to be epitaxial along the TiO_2 (110) orientation. However, there exists a large lattice mismatch, which causes an anisotropic strain imposed on the film.

The magnetic properties were studied by Vibrating Sample Magnetometry (VSM).

Figure 4.5 shows the hysteresis loops measured with VSM at room temperature.

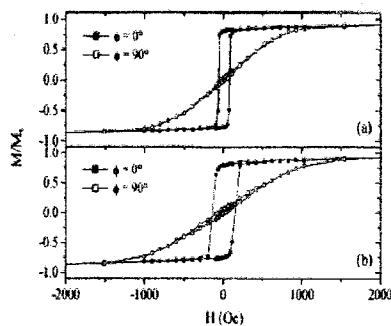


Figure 4.5: Hysteresis loops along (a) (100) and (b) (110) orientations [81]

As seen in Figure 4.5, the films are showing the anisotropic properties. The hysteresis loops are totally different along the easy axis and the hard axis. The magnetization switching behaviors are also different for different orientations of the external fields. For the external field that is along the hard axis, the switching mechanism is dominated by coherent rotation. For the external field that is off the hard axis, the nucleation of the domain wall happens in the magnetization reversal process.

The saturation magnetization is 475 emu/cm^3 at room temperature. According to the theoretical prediction, it should be 500 emu/cm^3 . However, CrO_2 is a metastable phase in room temperature. The surface of the sample can easily decompose into CrO_3 and the total saturation magnetization is reduced.

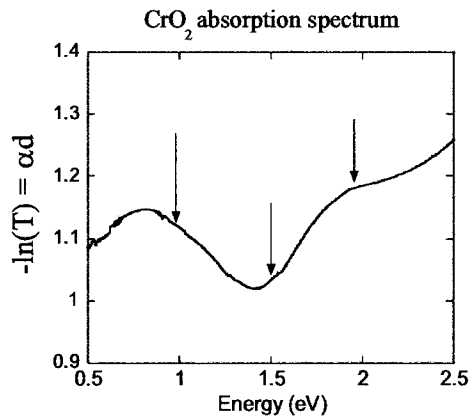


Figure 4.6: The optical absorption of one of the samples (provided by NIST). The arrows indicate important transitions.

The absorption of our films, as shown in Figure 4.6, shows the same general fea-

tures as those published [23, 72]. There are two significant features: one around 1 eV which Korotin et al assign to transitions between the t_{2g} bands, and a second feature beginning to peak around 2 eV which corresponds to the minority band transitions. These features will become important in the discussion of Chapter 5.

Another epitaxial thin film of CrO_2 , grown by CVD, was used for the magnetization rotation studies. It was provided by and characterized by Dr. Ale Lukaszew at the University of Toledo, in collaboration with Idelfonso Guilaran at Earlham College, Indiana. The CVD technique used was developed by Ivanov et al. [99]. The films were determined to be epitaxial by x-ray diffraction with a thickness of about 175 nm.

Figure 4.7 shows the coercivity of the hysteresis loops as a function of c -axis applied field angle. Clear uniaxial anisotropy is seen.

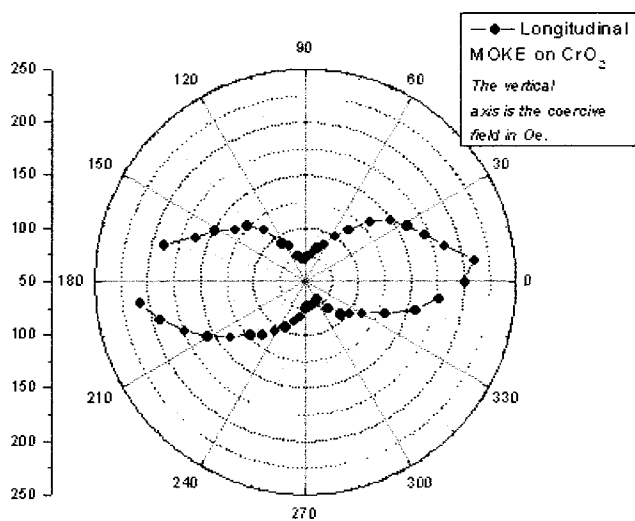


Figure 4.7: Coercivity versus applied field angle taken from MOKE curves, provided by Dr. Ale Lukaszew.

Chapter 5

Ultrafast Spectroscopy of CrO₂

As mentioned in the previous chapters, pump-probe spectroscopy has been a very important technique to study the dynamics of materials. In this chapter, studies of ultrafast pump-probe ultrafast transmission on CrO₂ thin films are presented. The behavior of the pump-probe transmission was studied as a function of temperature, wavelength and polarization of the probe. We have observed optical anisotropy which is consistent with the Cr-3d and O-2p bands hybridization model. A ~ 200 -600 picoseconds decay process was observed and was attributed to the spin relaxation. The wavelength and temperature dependent measurements imply there is a band gap of $1.5 \sim 2$ eV near the Fermi surface, consistent with recent calculations. This study shows that important features of bandstructure and magnetization of CrO₂ can be studied using ultrafast transmission experiments.

5.1 Background

CrO₂ has attracted much attention recently because of its newly discovered half-metallic property [1, 2, 3]. In Chapter 2, the half-metallic property of CrO₂ was introduced. The half-metallic property of CrO₂ deeply affects the transport properties

of the material and makes it a potential candidate for spintronic devices and spin injectors [4, 5]. It is also expected that the half-metallic properties would affect the optical absorption.

As was discussed in Chapter 2, half metallic CrO_2 is a transition metal oxide with rutile structure and lattice constants of $a=b=4.421 \text{ \AA}$ and $c=2.916 \text{ \AA}$ [100]. It is a ferromagnetic metal below the Curie temperature (386 K). The magnetic easy axis is along (001) direction (corresponding to the c-axis). The Cr^{4+} ion has a complete Ar shell plus two 3d electrons. Correspondingly, each O^{2-} ion in the crystal has a He shell plus six 2p electrons. At the oxygen sites, the crystal field leads to two sp^2 combinations formed by the 2s and $2p_x$, $2p_z$ electrons, and a $2p_y$ state whose orbital plane is perpendicular to c-axis. For the chromium sites, the crystal field splits the 3d bands into three t_{2g} states and two e_g states. In the local coordinate system, the 3 t_{2g} orbitals can be expressed as the natural base $3d_{xy}$, $3d_{xz-yz}$ and $3d_{xz+yz}$. One of the t_{2g} states, namely $3d_{yz-xz}$, is hybridized with the oxygen $2p_y$ state and forms an π -type state near the Fermi level [23, 54]. The strong orbital anisotropy has been previously investigated with optical spectroscopy [55] and polarization-dependent x-ray absorption spectroscopy [54].

Band structure calculations have been performed using different approximations [22, 23, 24]. Although they are different in details, the main results in the vicinity of Fermi level are similar: One of the two 3d electrons occupies the $3d_{xy}$ state, which is localized and forms a spin up “core”. Another 3d electron partly fills the $\text{Cr-}3d_{yz+xz}$ band and the hybridization band of the $\text{O-}2p_y$ and $\text{Cr-}3d_{yz-xz}$, and is

itinerant. It propagates through the spin up “cores” and aligns its spin with them resulting in a double exchange mechanism.

One of the difficulties in studying the bandstructure and electronic and spin dynamics of CrO_2 is that it is metastable at 300 K in air and the top 1-2 nm of the thin films rapidly decomposes into an amorphous state with a stoichiometry similar to antiferromagnetic Cr_2O_3 . Recently, ultrafast laser pump-probe spectroscopy has been used to study spin and magnetization dynamics in CrO_2 [12] as well as other half-metals [11]. Studying thin films by optical transmission should minimize surface effects. To investigate the electronic structure of CrO_2 , we have performed polarization-dependent ultrafast spectroscopy on anisotropic CrO_2 thin films at different temperatures for different wavelengths. Our results are consistent with the band structure calculations, which predict strong orbital anisotropy.

5.2 Experiment

The films studied were ~ 500 nm thick epitaxial CrO_2 grown by thermal decomposition of CrO_3 powder on TiO_2 (110) substrates. The details of film growth and characterization can be found in Chapter 4 and from one of our collaborator’s publications [81]. For transmission experiments, both sides of the TiO_2 were polished.

The ultrafast dynamics were measured by pump-probe experiments, as outlined in Chapter 4. The sample is excited by a pump laser pulse, and measured by a delayed probe pulse. A mode-locked amplified Ti:Sapphire laser, with 1 kHz repetition rate and 150 fs duration, was used as the pump. The wavelength of the pump beam was

800 nm (1.5 eV). The probe beam was tuned to various wavelengths: 650 nm (2.0 eV), 800nm (1.5 eV) and 1300 nm (1.0 eV). The 1300 nm pulses were obtained from an optical parameter amplifier (OPA). The 650 nm pulses were obtained by doubling the frequency of the 1300 nm pulses using a BBO crystal. The pulse energy for the pump and probe were approximately 20 μJ and 10 nJ, respectively. The beam size of pump and probe are about 10 mm² and 1 mm², which gives a fluence of 0.06 mJ/cm² and 0.3 $\mu\text{J}/\text{cm}^2$, respectively. The probe beam transmitted through the sample was measured by a silicon photodiode. The pump beam was chopped at 400 Hz and the differential transmission signal was measured by lock-in amplifier. The sign of the differential transmission was determined by setting the phase by the pump beam. The sign (induced absorption or transmission) was confirmed by checking the response of a gold film. The experiments were conducted at various temperatures from 300 K to 440 K.

5.3 Results and Discussion

The differential transmission results show a wavelength and polarization dependence of the probe beam, as shown in Figure 5.1. In this figure, the differential transmission ($\Delta T/T$) is shown at 300 K for the pump at various energies (wavelengths) and for polarizations parallel or perpendicular to the c-axis. As shown in Figure 5.1 a and Figure 5.1 b, the pump causes a greater increase in absorption ($\Delta T < 0$) of the probe beam whose polarization (E) is perpendicular to the c-axis than for the case of a probe polarization parallel to the c-axis ($\Delta T < 0$ for 1.5 eV and $\Delta T > 0$ for 1 eV). For a 2 eV

probe energy, shown in Figure 5.1 c, the opposite is true. The pump beam decreases the absorption ($\Delta T > 0$) of the probe beam with polarization perpendicular to the c-axis while increasing the absorption of the probe whose polarization is parallel to the c-axis. The specific polarization or wavelength of the pump beam does not have a noticeable effect on the signals.

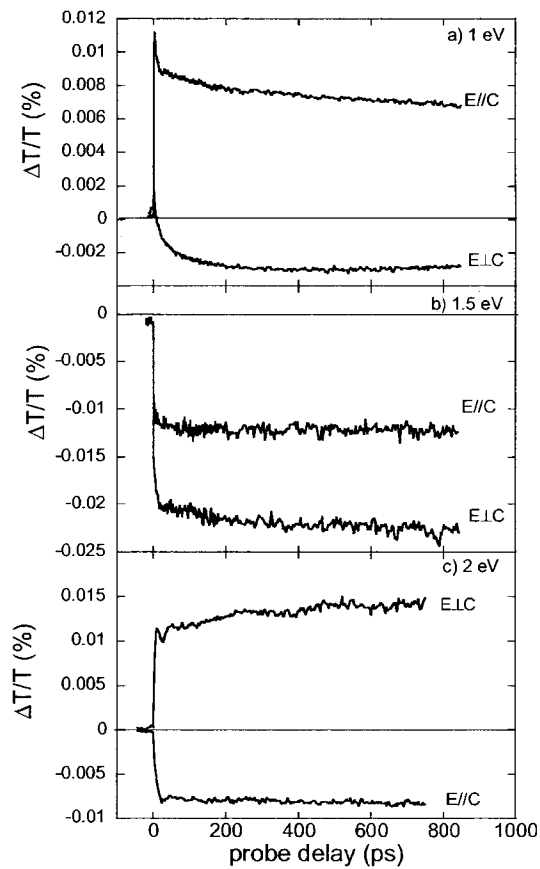


Figure 5.1: Pump-probe differential transmission at 300 K with probe energy of (a) 1 eV, (b) 1.5 eV, and (c) 2 eV. The probe polarization is either parallel or perpendicular with the crystal axis, as indicated.

The differential transmission signals studied as a function of temperature show

abrupt changes around the Curie temperature of the CrO₂, as shown in Figure 5.2 and Figure 5.3, indicating that the behavior seen is related to the magnetic properties. For the probe energy at 1 eV with E⊥c, as shown in Figure 5.2 a, the differential transmission signal shows a pump-induced increase in absorption which increases in magnitude up until T~T_c, after which the signal decreases to zero. In Figure 5.2 b the signal for the probe energy at 2 eV with E⊥c is shown, for increasing temperatures from 300 to 440 K. The signal drops abruptly with increasing temperature and disappears at and above the Curie temperature. This behavior can be qualitatively represented by a plot of ∂α/∂T, shown in Figure 5.3. The absorption change relative to temperature T is determined by:

$$\frac{\partial\alpha(\omega)}{\partial T} = -\frac{1}{L} \left[\frac{1}{\mathcal{T}(\omega)} \frac{\partial\mathcal{T}(\omega)}{\partial T} + \frac{1}{1-\mathcal{R}(\omega)} \frac{\partial\mathcal{R}(\omega)}{\partial T} \right] \quad (5.1)$$

Where

$$\exp(\alpha(\omega) \cdot L) = \frac{\mathcal{T}(\omega)}{1-\mathcal{R}(\omega)} \quad (5.2)$$

in which $\mathcal{T}(\omega)$, $\mathcal{R}(\omega)$ and $\alpha(\omega)$ are transmission, reflectivity and absorption coefficient respectively. T is the temperature and L is the thickness of the sample. Since the transmission change $\Delta\mathcal{T}(\omega)$ is small, we can take

$$\frac{\partial\mathcal{T}(\omega)}{\partial T} = \frac{\Delta\mathcal{T}(\omega)}{\Delta T} \quad (5.3)$$

where ΔT is the temperature change due to the pump pulse. Considering $(T(\omega) \ll$

$1 - R(\omega)$, Equation 5.1 can be simplified as:

$$\frac{\partial\alpha(\omega)}{\partial T} = -\frac{1}{L\Delta T} \frac{\Delta T(\omega)}{T(\omega)} \quad (5.4)$$

In our experiments, $(\Delta T(\omega)/T(\omega))$ is the measured value. Using Equation 5.4, $\partial\alpha(\omega)/\partial T$ was calculated from Figure 5.2 and plotted in Figure 5.3. Each data point is an average over the range from 600 ps to 700 ps since the change of the signal is small in this range. In Figure 5.3a, the signal for the probe at 1 eV, with $E \perp c$ is shown. The temperature dependence of this signal shows a “ λ ” shape around the Curie temperature. The 2 eV probe with $E \perp c$, however, experiences a pump-induced decrease in absorption which decreases as the temperature increases, as shown in Figure 5.3b. For the $E \parallel c$ cases the absorption decreases as the temperature increases. For the 1.5 eV data, both the $E \perp c$ and $E \parallel c$ configurations give an increasing absorption as the temperature increases, which indeed is consistent with the temperature dependent absorption measurements [73].

In Figure 5.2a, a long term decay of a few hundreds picoseconds (depending on the temperature) was observed for the temperature below T_c . We believe this is a spin flip process because this decay disappears above the magnetic phase transition temperature. The decay time of this process depends on temperature, which is also observed in the colossal magnetoresistant manganites [101]. Since the pump beam was kept same in all the experiments, this spin flip process should also be evident when the probe is at 800 nm and 650 nm, although our data suggest that these are not the optimal wavelengths to elucidate this process.

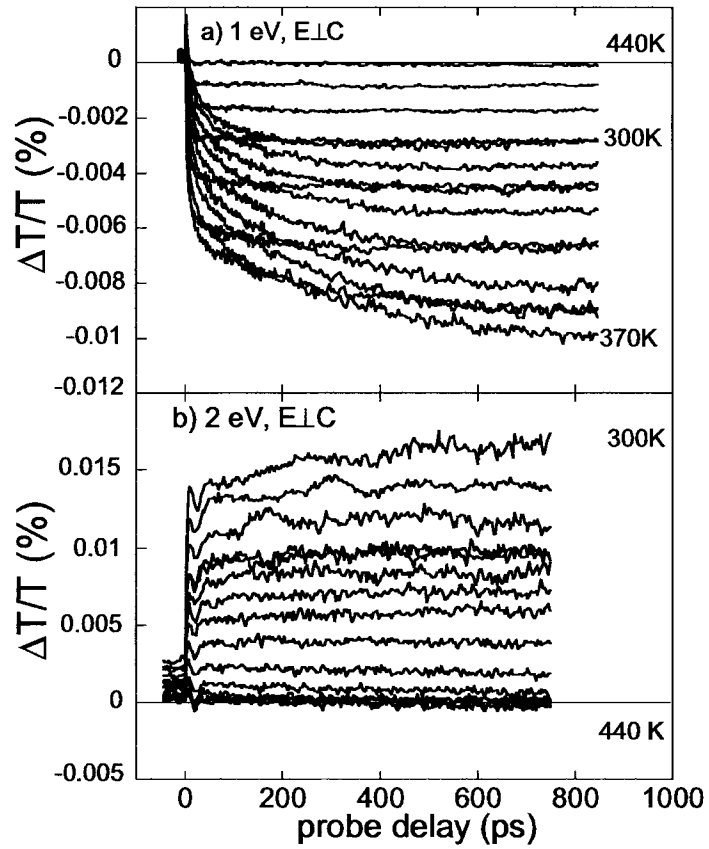


Figure 5.2: Pump-probe differential transmission at various temperatures from 300 K to 440 K for probe polarization perpendicular to the c axis, with a probe energy of (a) 1 eV and (b) 2 eV. In (a), the differential absorption increases from 300 K up to approximately 370 K, and decreases to zero afterwards. In (b), there is a continuous decrease of the differential transmission signal to zero from 300 to 440 K.

The optical anisotropy revealed in these experiments is consistent with the general features of the CrO_2 bandstructure. The π -type state formed by the hybridization of oxygen P_y state and the chromium d_{xz-yz} state is expected to play an important role in the differential transmission anisotropy. It is close to the Fermi surface and thus can be easily excited optically. Its orbital, as we have discussed, is perpendicular with the c -axis and thus the electrons in the band are more sensitive to the laser pulse with $E \perp c$ because the E vector is in the orbital plane. Moreover, this π -type state is also the origin of the anisotropy of X-ray absorption spectroscopy (XAS) and the X-ray magnetic circular dichroism (XMCD) [54, 76].

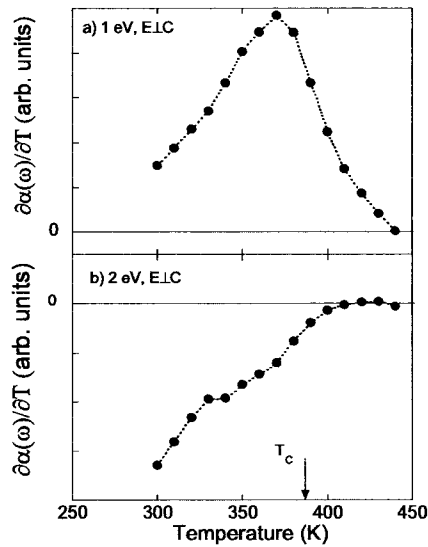


Figure 5.3: Behavior of the differential absorption as a function of temperature for probe polarization perpendicular to the c axis, with a probe energy of (a) 1 eV and (b) 2 eV. The differential absorption change is determined from the differential transmission shown in Figure 5.2, averaged from 600 to 700 ps, as described in the text. Note the characteristic “ λ ” shape around the Curie temperature in (a) and the decrease of the signal to zero in (b).

The fact that 2 eV probe with $E \perp c$ is less absorbed than the $E \parallel c$ probe while 1 eV and 1.5 eV probes of $E \perp c$ are more absorbed than the $E \parallel c$ probe pulses can be explained by assuming this π -type band as the upper level of the 1 eV and 1.5 eV optical transitions and the lower level of the 2 eV transition. This assumption is strongly supported by the temperature dependent optical absorption experiments [73]. According to this assumption, the electronic population of the π -type state is important to the 1 eV, 1.5 eV and 2 eV transitions. The pump pulse heats the electrons, shown in Figure 5.4, and redistributes them near the Fermi level. More empty states are then created in the π -type band, which is situated near the Fermi surface. The increase of the empty states in the π -type band enhances the 1 eV and 1.5 eV optical transitions, whose final states are in the band, and decreases the absorption of the 2 eV photons because of the electronic population decrease.

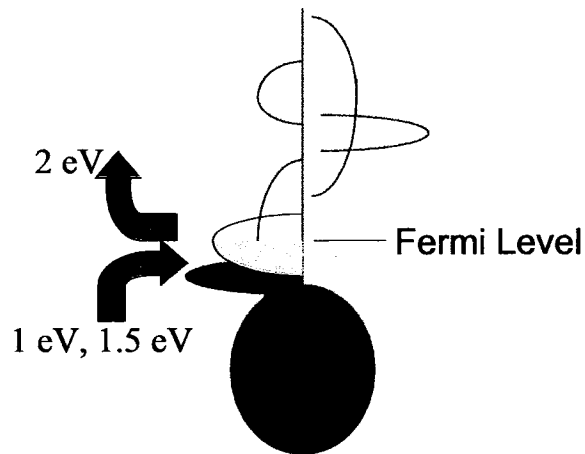


Figure 5.4: Schematic of the density of states (DOS) near the Fermi surface

This picture is confirmed by the temperature dependence of the signals (Fig-

ure 5.3). For example, in Figure 5.3b, $\partial\alpha(\omega)/\partial T$ is negative, which means the absorption coefficient decreases as the temperature increases. If we take the absorption as an indication of the electronic population, we can easily see the reasonable result that the electronic population at the energy level near the Fermi surface is decreased by the rising temperature.

The “ λ ” shape shown in Figure 5.3a is a characteristic shape of specific heat near the magnetic phase transition [102]. Here if we assume the 1300 nm optical transition is an intraband transition, then all the absorbed photon energy is converted to heat. Therefore it is reasonable to expect at this wavelength the absorption coefficient has a similar feature with the thermal properties of the material near the magnetic phase transition temperature. Although not very prominently, the same “ λ ” shape is also observed in the 1.5 eV experiments. But no such curve is observed in the 2 eV case (Figure 5.3b). This implies that the 1 eV and 1.5 eV transitions are the intraband transitions in which most of the absorbed energy is converted to the form of heat, while a large part of the energy absorbed in the 2 eV transitions produces interband excitations and thus the “ λ ” shape of the specific heat is not evident. Instead, we see an absorption related with the electronic population. Therefore, we believe there is a band gap of about 1.5~2 eV near the Fermi surface that separates the interband and intraband transitions. This gap could be the predicted minority gap [23, 76].

5.4 Summary

In summary, we have performed ultrafast transmission measurements on anisotropic CrO₂ thin films. We have observed optical anisotropy which is consistent with the Cr-3d and O-2p bands hybridization model. A ~ 200 -600 picoseconds decay process was observed and was attributed to the spin relaxation. The wavelength and temperature dependent measurements imply there is a band gap of 1.5~2 eV near the Fermi surface.

Further work should be done to develop a quantitative model to describe the above data. A starting point is the diagram of proposed transitions shown in Figure 5.4.

Chapter 6

Spin Lifetimes of CrO₂ Probed by Ultrafast MOKE

The spin freedom of the electrons has long been neglected in traditional electronic applications. Only recently have the manipulation and the detection of the electron spins started to attract interests of scientists [103, 104, 105], due to the newly discovered application of the electron spins in information technology. This recently developed research area is sometimes called “spintronics”. The traditional electronic devices only use the charge of the electrons to deliver information, while “spintronic” devices use both the charge and the spin of the electrons to deliver information.

To effectively deliver information using “spintronic” devices, one needs to know how to generate a net spin polarization, keep it while delivering, and detect it. Thus, information can be attached to an electron in a form of spin “up” or spin “down”, and be transferred to the detector. This makes the spin lifetime of materials of critical importance for spintronics. In this chapter, the spin lifetime of half metallic CrO₂ is discussed, because it is very important to the spin transfer properties of the material. The longer the spin lifetime is, the easier the net spin polarization can be reserved while the electrons are delivered to the detector. The measurements presented here are first to show that the magnitude of magnetization can be directly modified by

an ultrafast pump. In addition, the behavior of the spin lifetime near the Curie temperature is discussed.

6.1 Introduction

In magnetic metals, the flipping of spins is believed to be mainly due to the spin-lattice coupling, and the spin relaxation time depends on the type and amount of lattice defects [106]. The spin flip mechanism of semiconductors is more complicated, considering the complexity of semiconductors themselves. Types of carriers, defects and doping are all factors that might affect the spin relaxation time.

There has not been a generally accepted theory about the spin relaxation of half-metallic materials, probably due to the lack of the experimental data. But it is legitimate to fit half-metallic data by spin relaxation theory of ferromagnetic materials in most cases, because most of half-metallic materials are ferromagnetic. A group at the University of Tokyo [11] exploited ultrafast MOKE to study the spin relaxation of half-metallic $\text{Sr}_2\text{FeMoO}_6$. The MOKE system was set to polar configuration, and a pulsed laser system was used to measure the transient MOKE signal change of $\text{Sr}_2\text{FeMoO}_6$ sample. It was observed the spin relaxation time of this sample at different temperatures fit very well into the 3D Ising model or 3D Heisenberg model, which in return proved the validity of applying ferromagnetic spin relaxation theory to half-metallic materials.

6.2 Experiment

In our experiments, we use a polarizer-analyzer pair, instead of the balanced detector, in the detecting system. And we set our MOKE system to longitudinal configuration. The experimental results of spin relaxation that are similar with half-metallic $\text{Sr}_2\text{FeMoO}_6$ were obtained in our ultrafast MOKE measurements. Figure 6.1 shows the basic setup.

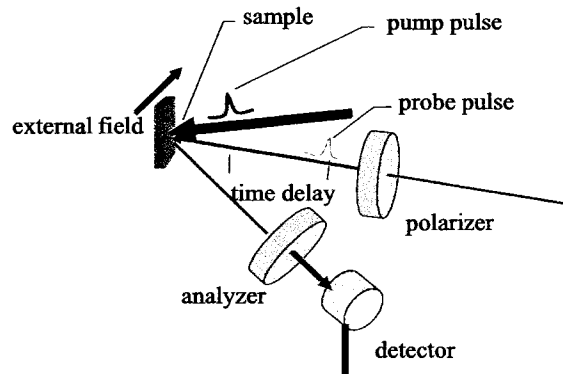


Figure 6.1: Ultrafast MOKE setup

A heater was used to control the temperature of the sample. Static MOKE was measured by chopping the probe beam, ultrafast MOKE by chopping the pump beam and detecting this frequency of signal on the lock-in amplifier. The strength of the pump beam was approximately 40 nJ, and the probe beam was about 10 nJ. The time delay between the pump and the probe was controlled by a motion stage. The samples studied were ~ 500 nm thick and were grown in NIST [81].

6.3 Results

Using pump pulses of energy of approximately 40 nJ, we are able to see a change in the magnitude of the magnetization, as probed by MOKE. This is similar to the experiments which have been done in Ni [15]. This is not surprising that this can be seen, since the Curie temperature in CrO_2 is so low.

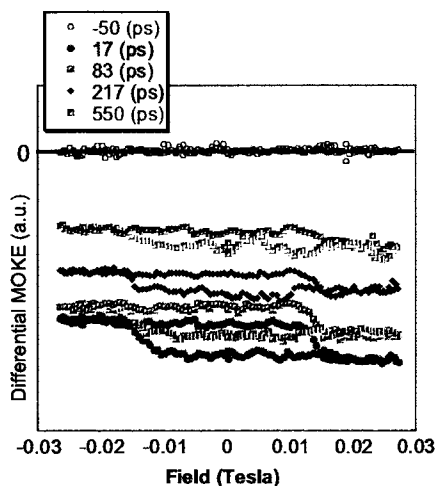


Figure 6.2: Dynamic MOKE signal for various delay times

Figure 6.2 shows MOKE curves taken with the probe beam, while locking in on the frequency of the chopped pump beam (dynamic or ultrafast MOKE), for several time delays. If the probe arrives before the pump, no change is seen in the MOKE curve (e.g., no signal is seen), as would be expected. For increasing probe delays after the pump, by sweeping the magnetic field, hysteresis loops are measured, indicating a pump-induced change in the magnetization.

Figure 6.3 shows the dynamic MOKE signal (again, from locking in on the chopped

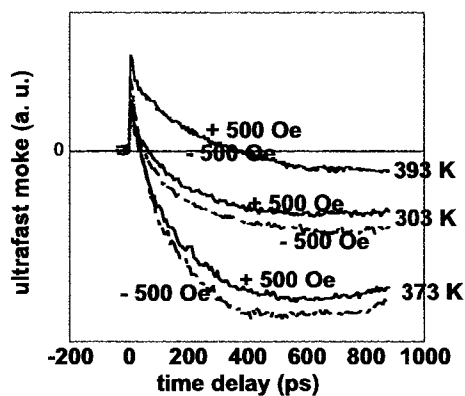


Figure 6.3: Ultrafast MOKE results

pump frequency) as a function of pump-probe delay for three temperatures around the Curie temperature and for applied fields of +500 Oe or -500 Oe, which were enough to saturate the magnetic moment of the film. The pump pulse hits the film to raise the electron temperature in a very short time, and the probe pulse follows to measure the change of the magnetic moment using the MOKE effect.

In Figure 6.3, the longitudinal transient MOKE results at 303 K, 373 K and 393 K are displayed. Notice that the Curie temperature of CrO_2 is 386 K. It is obvious the external magnetic field has no effect on the sample as the temperature is higher than the Curie point. While as the temperature is lower than the Curie point, the transient MOKE curves bifurcate for +500 Oe external field and -500 Oe field.

Ideally, for positive and negative fields, the transient MOKE curves should be symmetric, i.e., if the -500 Oe gives a negative curve, +500 Oe should give a positive curve that is an exact inversion of the negative one. However, since the transient

change of reflectivity is inevitable in our experiments, the transient MOKE curves we obtained are actually mixed with the transient reflectivity change. One way to get rid of the reflectivity component is to subtract the +500 Oe MOKE signal from the -500 Oe MOKE signal. Figure 6.4 is a diagram showing the results of the subtraction, which we label the differential MOKE curve.

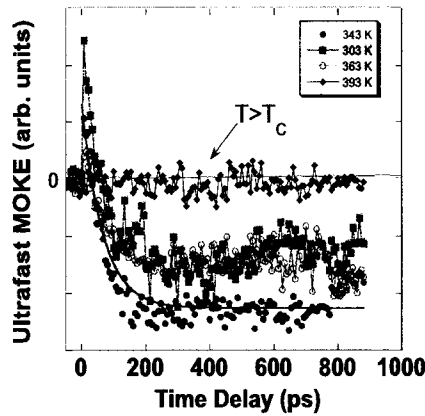


Figure 6.4: Differential MOKE curves for four different temperatures, found by taking the difference of the curves at + and - applied fields in Figure 6.3. The differential MOKE curve disappears above the Curie temperature (T_c). The solid line for the 343 K data is a fit to an exponential dependence, revealing the spin relaxation time, as discussed in the text.

In Figure 6.4, the differential MOKE curves are shown at different temperatures. As the temperature is lower than 380 K (that is, below the Curie point), the differential MOKE signal is obvious; as the temperature is higher, the differential MOKE signal becomes zero. We would expect this to happen if we are probing the magnetization, and hence the spin dynamics, by differential MOKE. The differential MOKE curves appear to show the main features seen in the half-metallic material $\text{Sr}_2\text{FeMoO}_6$: a relaxation to a quasi-equilibrium state on a timescale of about 100 ps, followed by

and a very long scale relaxation to the initial (unexcited) state. Kise et al. modeled this behavior in $\text{Sr}_2\text{FeMoO}_6$ by assuming the Kerr signal took the form:

$$\Delta S_{Kerr} = (\Delta S_{max} - \Delta S_{step})(1 - \exp(-t/\tau_{spin})) \quad (6.1)$$

where ΔS_{max} and ΔS_{step} are the maximum (quasiequilibrium) change and initial (instantaneous) change in the Kerr signal and τ_{spin} is the spin relaxation time. A fit to this dependence is shown for the data at 343 K in Figure 6.4, yielding $\tau_{spin} = 65$ ps. Again, the general behavior of the Kerr signal appears to be similar to that seen in $\text{Sr}_2\text{FeMoO}_6$. However, what is not similar to the experiment in $\text{Sr}_2\text{FeMoO}_6$ is the temperature dependence of the spin relaxation time. In $\text{Sr}_2\text{FeMoO}_6$, a very obvious increase in spin relaxation time (by over an order of magnitude) was seen as the temperature approached the Curie temperature. For the data in Figure 6.4, no such dramatic increase is seen.

We are unclear as to why we are not seeing a dramatic increase in spin relaxation time as seen in the other half-metallic system $\text{Sr}_2\text{FeMoO}_6$. One possibility is our detection of longitudinal MOKE (proportional to the Kerr angle) as opposed to Kerr ellipticity, as was done by Kise et al.. To further explore the nature of spin relaxation time in CrO_2 , we turn to differential absorption data, presented in the previous chapter.

In Chapter 5 we presented data that shows that for a probe tuned to 1 eV energies, pump-probe transmission signals are obtained which appear to be connected to the magnetization. Figure 6.5 is the infrared transmission results that we have seen in

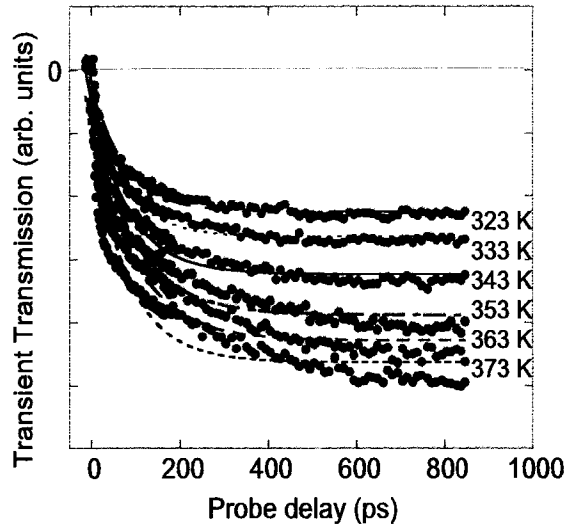


Figure 6.5: Differential transmission signals for a 1 eV probe for different temperatures approaching the Curie point. The signal disappears at the Curie temperature. The lines are fits to a single exponential, as was used for the differential MOKE and by Kise et al.. The signal obviously does not contain a single decay component, especially at higher temperatures

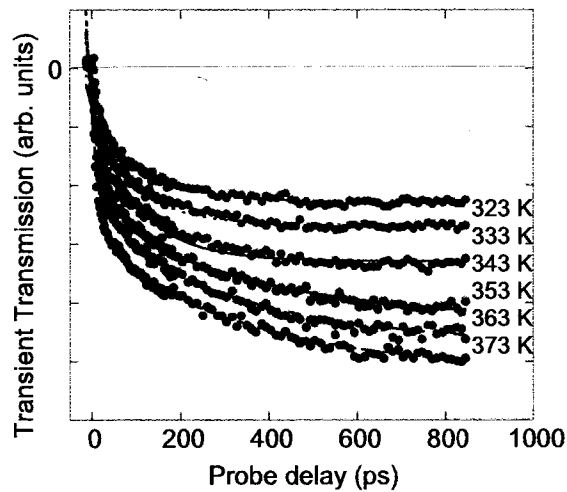


Figure 6.6: The data presented in Figure 6.5, but with fits including a second decay time (a second exponential). The fits are much better, indicating two decay components.

the last chapter below the Curie temperature. Here we will focus our attention on the shape of the curves instead of the average values of the pump induced transmission change. The reason is that the spin decay process is in the range of 10 - 1000 picoseconds and it is observable from the shape of the curves in this range. As the temperature increase towards the Curie temperature, the decay time for the differential transmission curves become obviously longer (the approach to equilibrium takes longer). Assuming that the differential transmission signal at 1 eV is a probe of spin dynamics (since it disappears above the Curie temperature), we fit the differential transmission data to a single exponential indicating spin relaxation time. The fits are shown in Figure 6.5. It is obvious, especially at higher temperatures, that the fits are not good, and that there is more than one decay component for these signals. Figure 6.6 shows fits including a second decay term; the fits are very good for this case. Figure 6.7 shows a plot of the two extracted relaxation (decay) times as a function of temperature. One time is seen to be increasing, while the shorter time is decreasing. The longer time could be the spin relaxation time, as we expect it to increase while approaching the Curie temperature.

6.4 Summary

In summary of this chapter, the spin activities of half-metallic CrO_2 were studied. The differential MOKE signal was detected, showing that the magnitude of the magnetization could be affected by the pump beam. Differential MOKE curves showed, near the Curie temperature, a long lived excitation, but it was difficult to extract

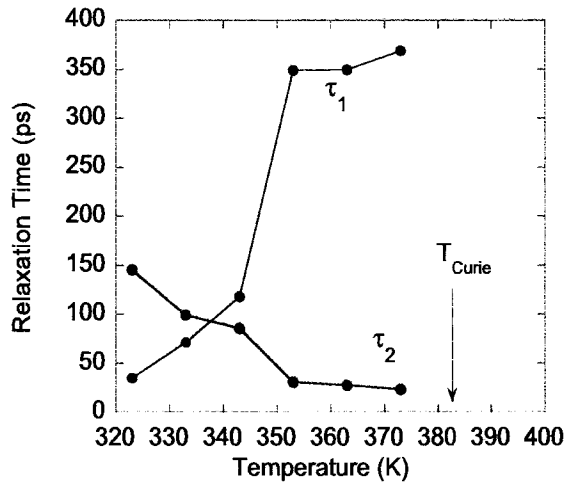


Figure 6.7: The temperature dependence of the two extracted relaxation times from the fits in Figure 6.6. The lines are a guide to the eye.

spin lifetimes from these measurements. Perhaps using longitudinal MOKE causes the difficulties. Future experiments should probe the ellipticity as the experiments of Kise et al.. In contrast, it appears that spin lifetimes can be extracted from the pump-probe transmission. The spin decay time of hundreds of picoseconds was observed.

Chapter 7

Coherent Magnetization Oscillation in CrO₂ and Temperature Dependent Study of Magnetic Anisotropy

Recently, ultrafast pump-probe measurements of magnetization dynamics have shown the excitation of coherent magnetization oscillations or spin waves in several classes of materials. These oscillations have been used successfully to study magneto-crystalline anisotropy. In this Chapter, we apply this ultrafast technique to study the temperature dependent anisotropy in CrO₂. We find clear oscillations for the condition where the externally applied magnetic field is perpendicular to the direction of the magnetic easy axis, similar to results by Zhang et al. [12]. The oscillations quickly disappear as the angle between the magnetic field and easy axis is decreased from 90°. Zhang et al. were the first to report the observation of coherent oscillations in CrO₂ and to model them using the LLG equation, as well as show that multiple pulses could achieve coherent control of the oscillations. We expand upon this study by measuring the oscillations over a range of applied magnetic fields and over a temperature range of 10 - 360 K. For higher temperatures, we find that the oscillations are well described by a single exponentially decaying sinusoidal. The oscillation frequency as a function of applied field strength is fit using a modified LLG model. It is found that

anisotropy constants comparable to those measured by other techniques can be extracted, if a contribution due to strain anisotropy is included. At lower temperatures, the oscillations can not be fit well by a single sinusoidal. The general dependence of the anisotropy constants on temperature extracted from these fits will be discussed.

7.1 Background

Anisotropy is a feature of crystalline ferromagnetic materials. Without crystalline structure, the exchange energy between neighboring spins depends only on the relative orientation between spins. In a crystalline structure, however, the magnetic behavior is strongly dependent on the relative orientation between the magnetic moments and the crystalline axes. For materials such as 3d transition metals, where the magnetization is due to electron spin, spin-orbit coupling is responsible for this dependence. The spin-orbit coupling gives rise to favored orientations of spins, known as easy axes. Unfavorable directions of magnetization are known as hard axes.

The simplest type of anisotropy is uniaxial magnetic anisotropy. In this case, there is one easy axis along which the magnetization prefers to lie. The magnetocrystalline anisotropy energy can be described in terms of the angle between the magnetization and the easy axis direction:

$$\epsilon_a = K_{u1} \sin^2 \theta + K_{u2} \sin^4 \theta + K_{u3} \sin^6 \theta + \dots \quad (7.1)$$

The terms K_u are anisotropy constants, and they are of different orders. The common 3d ferromagnet Co displays uniaxial anisotropy, as well as CrO_2 . Cubic crystals such

as Ni and Fe display cubic anisotropy, which is described by direction cosines with respect to the three cube edges. For crystalline thin films, the magnetocrystalline anisotropy described above is the major source of anisotropy. Other sources include strain and interface effects due to lattice mismatch between the film and substrate. Also, the surface of the thin film may display different anisotropy than the bulk.

There are several methods for measuring anisotropy. Static methods include torque magnetometry and measurement of hysteresis loops by SQUID magnetometry or the magneto-optical Kerr effect. Dynamical methods include ferromagnetic resonance and Brillouin light scattering. For these techniques, the anisotropy is determined by the effect on the spin relaxation. A new dynamical measurement of anisotropy was developed over the last decade, involving an ultrafast pump-probe setup, as explained in Chapter 4. This technique has been shown to give measurements analogous to Ferromagnetic Resonance (FMR), specifically by Koopmans' group in 2002, and hence has been called "Optical FMR". One advantage of the technique is even low resonant frequencies can be measured precisely in the time domain and thus it expands the frequency range of the conventional FMR. Also, it is a local technique and does not require the sample to be uniform. The disadvantage of the technique is the detection of the signal could be hard for some materials. More details about the optical FMR technique can be found in Ref [107].

Figure 7.1 illustrates how the coherent magnetization oscillations are generated. An external magnetic field is applied perpendicular to the easy axis of the sample. The magnetization moment lies along the easy axis due to the magnetic anisotropy,

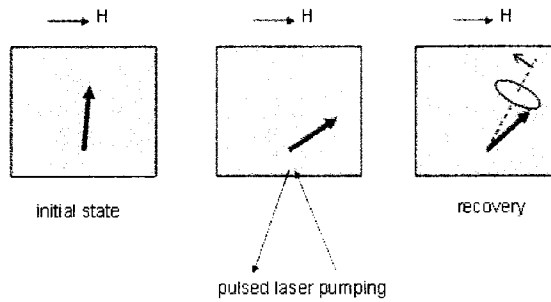


Figure 7.1: Demonstration of how coherent magnetization oscillations are generated although it's tilted a little under the influence of the external field. The incident pump laser pulse hits the sample and then significantly changes the magnetic anisotropy field, and the magnetic moment is excited to an off-equilibrium position due to the external field. In the recovery process, the magnetic moment rotates back to its initial position in a motion of precession. In the all-optical ultrafast experiment, the magnetization oscillations are detected by MOKE using a probe beam, as discussed in Chapter 4.

The exact mechanism by which the magnetocrystalline anisotropy is modified by the pump beam is still a topic of research. The pump pulse first excites the electronic system, which transfers energy to the spin system and ultimately the lattice. The temperature change in the electrons, spins and lattice can all effect the anisotropy. It is believed that the role of the different heating mechanisms varies for different materials [108, 109, 110, 111].

For CrO_2 , coherent magnetization oscillations were first reported by Zhang et al.. They modeled the oscillations using the LLG equations and showed that they could

reproduce the general features using the LLG equation. We expand on this study by conducting oscillation measurements over a range of magnetic fields and temperatures, and attempt to extract values for anisotropy directly from the oscillation measurements.

7.2 Experiment

The CrO_2 samples we used in the experiments was grown on TiO_2 substrate. The details of the growth are given in Chapter 4. The bulk CrO_2 has rutile structure with lattice constants $a=b=4.419 \text{ \AA}$ and $c=2.195 \text{ \AA}$. The lattice constants are slightly deviated from the bulk values for the epitaxial films where lattice mismatch between the CrO_2 and the rutile (TiO_2) substrate is considerably large. Significant strain effects, which are both temperature and thickness dependent, were found in these films and result in stress anisotropy.

Figure 7.2 shows the Scanning Electron Microscopy (SEM) picture of a sample. From the picture, one can estimate the thickness of the CrO_2 is about 175 nm. For the temperature dependent measurements, the sample was either positioned on a heater in air (for the temperature range 293 - 360 K) or was positioned in a magneto-optical helium cryostat for the temperature range (10 - 300 K).

The magnetization of the CrO_2 is shown in Figure 7.3. It can be seen that the CrO_2 has a definite easy and hard axis. Along the easy axis, the CrO_2 magnetization saturates at about 100 Oe, while along the hard axis, the magnetization saturates at 1500 Oe.

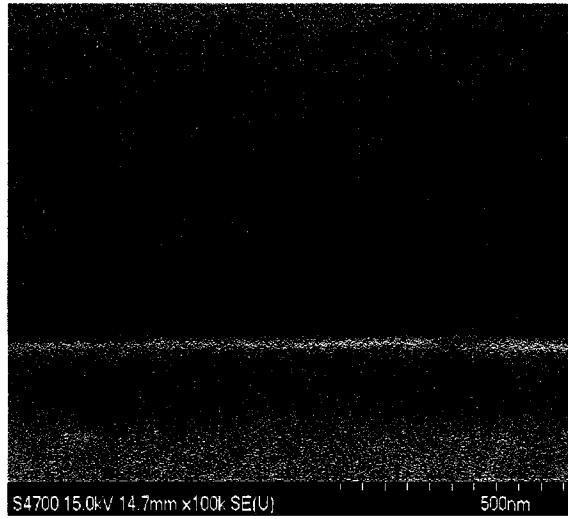


Figure 7.2: SEM image of CrO₂ thin film

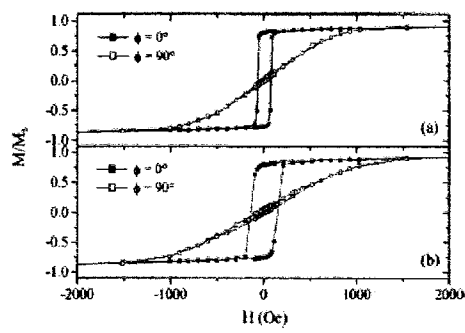


Figure 7.3: VSM Hysteresis loops of CrO₂ (a) (100) and (b) (110) thin film [81]

The details of the pump-probe coherent oscillation experiment are presented in Chapter 4. The pulse energy for the pump and probe were approximately 40 nJ and 10 nJ, respectively. The magnetic field is applied in the plane of the sample, along the hard axis (or, 90° from the easy axis). Coherent magnetization oscillations can be detected by MOKE in this configuration. Oscillation frequencies as a function of applied field were first studied in order to extract anisotropy constants at room temperature for comparison with other measurements. Then, a study of anisotropy as a function of temperature was conducted.

7.3 Room temperature anisotropy measurement

Figure 7.4 shows an example of coherent magnetization oscillations, detected by MOKE, at room temperature with an external magnetic field of 396 Oe applied along the in-plane hard axis. The oscillations are approximately single frequency, as is indicated by the fit to an exponentially decaying sinusoidal using an equation of the form:

$$A = A_1 e^{-t/T_1} + A_2 e^{-t/T_2} \sin(2\pi ft + \alpha) \quad (7.2)$$

Where T_1 and T_2 are the relaxation times, α is the initial phase, and f is the frequency. From the fit, a frequency of 5.33 GHz and decay times $T_1 = 350$ ns and $T_2 = 180$ ps are extracted. The longer decay time T_1 corresponds either to a long-term decay in the magnetization or base reflectivity signal (discussed in more detail in Chapter 6), while the time T_2 is a decay in the oscillation signal, related to the Gilbert damping parameter in the LLG equation describing decay of the coherent

magnetization oscillations. We also subject the time-domain data to a Fast Fourier Transform (FFT) (Kaleidagraph) to obtain the oscillation frequency. The FFT data is shown in the upper inset of Figure 7.4. Due to the relatively large damping, the number of the oscillations is limited and the FFT result has significant broadening. However, the center of the peak in Figure 7.4, the FFT is at 5.3 GHz, which is the same value extracted from the direct fit of the oscillations. For the following data analysis, the oscillation frequencies are extracted by a sinusoidal fit of the oscillation data.

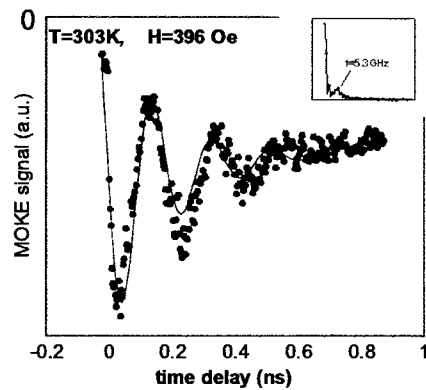


Figure 7.4: Coherent magnetization oscillations in CrO_2 at 303 K with an applied field of 396 Oe in plane along the hard axis. Solid line is fit to a decaying sinusoidal, as described in the text. Inset is FFT analysis, showing a single frequency component.

In Figure 7.4, one can observe from the data that the first period of the oscillation is shorter than the later ones, which is illustrated by the mismatch between the data and the fitting curve. This is probably due to the over pumping of the system and the pump pulse can no longer be considered as a perturbation. The same effect was

observed in Ref [12]. This is another reason why the FFT result has a broadening. However, this effect is not very strong and we can minimize its effect on the data by keeping the same pump power while obtaining data and using the same fitting function for each set of oscillations.

We also need to notice that the magnitude as well as the orientation of the magnetic moment could change if the pump power is too high. In our experiments we kept the pump energy as low as 1 mJ/cm² per pulse. The influence of the magnitude change of the magnetic moment was small comparing with the change of its orientation. More details about this are discussed in Chapter 6. We will only focus on the rotation of the magnetization moment in this data analysis.

Coherent magnetization oscillations can be seen up to a field of about 1000 Oe. For fields significantly higher than this, the oscillations can no longer be detected. We believe this is due to the fact that at higher fields the magnetic moment of the sample is largely deviated from the in plane easy axis. For example, with a 1000 Oe field applied along the hard axis, the magnetic moment of the sample will be 82° off the easy axis, as determined by hysteresis loop measurements. When the magnetization is essentially along the direction of the applied field, a pump-induced change in anisotropy will result in very small amplitude oscillations which cannot be detected. Similarly, there's no MOKE signal oscillation detectable for our set up when the external field is applied along the in-plane easy axis where the saturation field is very low. It is then easy to conclude that when the magnetic moment is along the direction of the external field, no oscillations should be detected.

The oscillation frequencies as a function of applied field at room temperature (T= 293 K) are shown in Figure 7.5. Unlike other systems (such as Koopmans' study of Ni), where the FMR frequencies have a simple square root-like relation with the applied fields, here the frequency decreases with the field applied along the in plane hard axis and then increases after a certain value. This “dip” is at the position near the anisotropy field.

We fit the data using an FMR based analysis of the LLG equations, as discussed in Chapter 3. Considering the strain effect due to the lattice mismatch, the free energy density can be written as:

$$\epsilon(\theta, \varphi) = -HM\cos(\varphi - \varphi_h)\sin\theta + \frac{H_d M}{2}\cos^2\theta + K_u\sin^2\varphi + K_\delta\sin^2(\varphi - \delta) \quad (7.3)$$

Where H is the applied field; M is the saturation magnetization; φ is the angle between the in plane magnetic moment and the easy axis; θ is the angle between the magnetic moment and the normal of the film; φ_h is the angle between the applied field and the easy axis; H_d is the demagnetization field; K_u is the uniaxial anisotropy constant, and K_δ and δ represent the stress anisotropy constants and its direction respectively. In our hard axis experiments $\varphi_h = \pi/2$ and $\theta = \pi/2$, the FMR frequency is calculated as:

$$f = \frac{g\gamma}{4\pi}\sqrt{(H\sin\varphi + H_d)[H\sin\varphi + (H_{K_u} + H_{K_{\delta c}})\cos 2\varphi + H_{K_{\delta b}}\sin 2\varphi]} \quad (7.4)$$

Where g is the Landau factor; $\gamma = 2\mu_B/\hbar$ is the electron gyromagnetic ratio; $H_{K_u} = 2K_u/M$ is the uniaxial anisotropy field; $H_{K_{\delta c}} = (2K_\delta/M)\cos 2\delta$ and $H_{K_{\delta b}} = (2K_\delta/M)\sin 2\delta$

represent stress anisotropy field along the c-axis and b-axis respectively. The direction of the magnetization ($\varphi = \varphi_0$) is determined by the equilibrium condition, or, by the minimization of the free energy (Equation 7.3):

$$2H \cos \varphi - (H_{K_u} + H_{K_{\delta c}}) \sin 2\varphi + H_{K_{\delta b}} \cos 2\varphi = 0 \quad (7.5)$$

The analytical fitting of the hard axis oscillation versus applied field data is impossible because Equation 7.5 does not have an analytical solution. We wrote a FORTRAN program to fit the data numerically (program is shown in Appendix B). The upper limits of $H_{K_u} + H_{K_{\delta c}}$, $H_{K_{\delta b}}$ and H_d were given and the program searches the region from zero to the upper limits of each of the above parameters. A root mean square (RMS) error is then defined for each set of the parameters. The program returns the combination of the parameters that gives the smallest RMS error.

For the data with a temperature of 303 K, the numerical fitting returns a combination of the parameters $H_{K_u} + H_{K_{\delta c}} = 778$ Oe, $H_{K_{\delta b}} = 63$ Oe and $H_d = 5688$ Oe. The solid line in Figure 7.5 shows the numerical fitting of the experimental data. Our fitting demonstrated the existence of strain anisotropy, for if there's no strain involved, the "dip" of the H-f curve will strictly touch the zero-frequency line. The dashed line in Figure 7.5 illustrates such an H-f curve by setting $H_{K_{\delta c}}$ and $H_{K_{\delta b}}$ to zero.

H_{K_u} and $H_{K_{\delta c}}$ are inseparable from the fitting of the data. However, we can estimate the value of $H_{K_{\delta b}}$ by assuming the anisotropy field is proportional to the lattice mismatch. The lattice mismatch of (100) epitaxial film on rutile substrate is

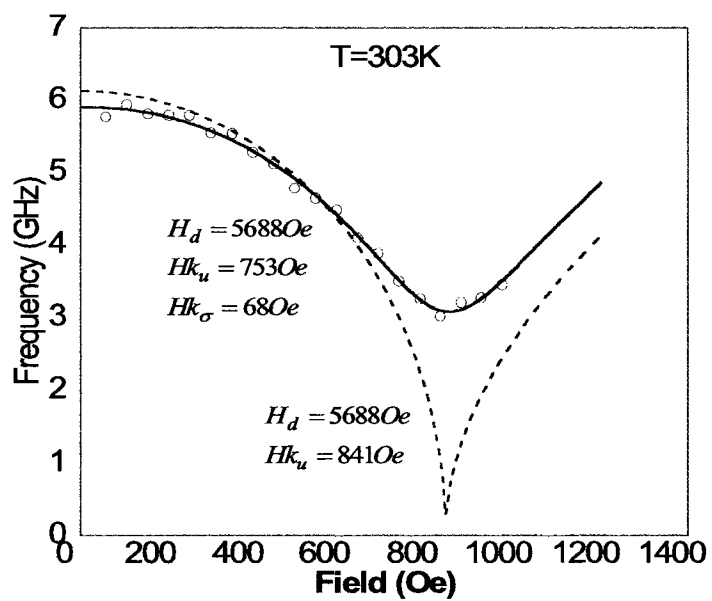


Figure 7.5: Oscillation frequencies extracted from magnetization oscillations at 303 K at different applied fields. Dashed line shows fit of data if strain is neglected, while solid line shows fit with strain term included. Numbers extracted from fits are shown

-3.79% and -1.48% along the b-axis and c-axis respectively. Then the direction of strain is 34.3° ($\delta = 34.3^\circ$) from the easy axis. $H_{K_{\delta c}} = 25$ Oe is evaluated by noticing $H_{K_{\delta b}} = 63$ Oe. And then $H_{K_u} = 753$ Oe is concluded. Table 1 shows the measured uniaxial anisotropy fields from different references. Our result is in good agreement with them. Using the equation $H_d = 4\pi M$ the saturation magnetization is calculated as $M = 453$ emu/cm³, comparing with the low temperature value of 650 emu/cm³. The uniaxial anisotropy constant $K_u = 1.70 \times 10^5$ erg/cm³ and the stress anisotropy constant $K_\delta = 1.54 \times 10^4$ erg/cm³ at the room temperature can be obtained. These results show that if a term due to strain anisotropy is included in the analysis, the all-optical pump probe measurements can allow for reasonable measurements of the uniaxial anisotropy of CrO₂.

| Source | Sample | Temperature | Method | H_{K_u} |
|---------------------------|-----------------|-------------|--|------------------|
| X. W. Li et al. [82] | 600 nm | 5 K | hysteresis measurements | 1350 Oe |
| F. Y. Yang et al. [80] | 500 nm | 300 K | hysteresis measurements | 830 Oe |
| L. Spinu et al. [83] | 200 nm | 300 K | rf. transverse susceptibility measurements | 600 Oe |
| B.Z.Rameev et al. [86] | 80 nm 150 nm | 300 K | FMR | 860 Oe 700 Oe |
| Our Work | 175 nm | 300 K | Optical FMR | 753 Oe |

Table 7.1: Comparison of our results with other measurements of anisotropy

7.4 Temperature dependent study of anisotropy

The temperature dependent properties of the anisotropies can be studied from the measurements of the oscillation frequencies at different temperature. One complicating feature, however, is that at temperatures below 250 K, the oscillations can no longer be well described by a decaying, single sinusoidal. Figure 7.6 shows coherent oscillations measured at 10 K, with the external field of 300 Oe. The oscillations cannot be fit by a single frequency function. The inset of the figure shows the FFT result of the oscillation, from which we can determine the frequency, but with large error due to broadening (with a full width at half maximum of about 2 GHz).

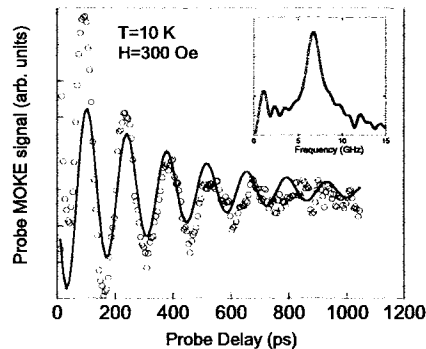


Figure 7.6: Magnetization oscillations at 10 K and applied field of 300 Oe. Inset shows an FFT of results, with a clear peak at about 6.7 GHz. The solid line in the Figure is a best fit to a single decaying sinusoidal. Notice the deviation of the data.

To study the temperature dependence of the anisotropy constants, we measured the oscillation from 10 K to 363 K (no oscillations were detected above 363 K). Figure 7.7 is a summary of the measured oscillation curves below room temperature. A general tendency observed is the oscillation frequency is lower for the higher temper-

ature measurements. This is a direct observation of the demagnetization field change and the anisotropy field change. Recalling Equation 7.4 of this chapter,

$$f = \frac{g\gamma}{4\pi} \sqrt{(H \sin \varphi + H_d)[H \sin \varphi + (H_{K_u} + H_{K_{\delta c}}) \cos 2\varphi + H_{K_{\delta b}} \sin 2\varphi]} \quad (7.6)$$

We see that a decrease of the frequency f implies either the decrease of the demagnetization field H_d or the decrease of the anisotropy field H_{K_u} and $H_{K_{\delta}}$. The quantitative analysis of the change can be studied by numerical fittings of the data. The fitting method was introduced in the previous part of this chapter. FFT analysis is used to extract the frequencies from these plots.

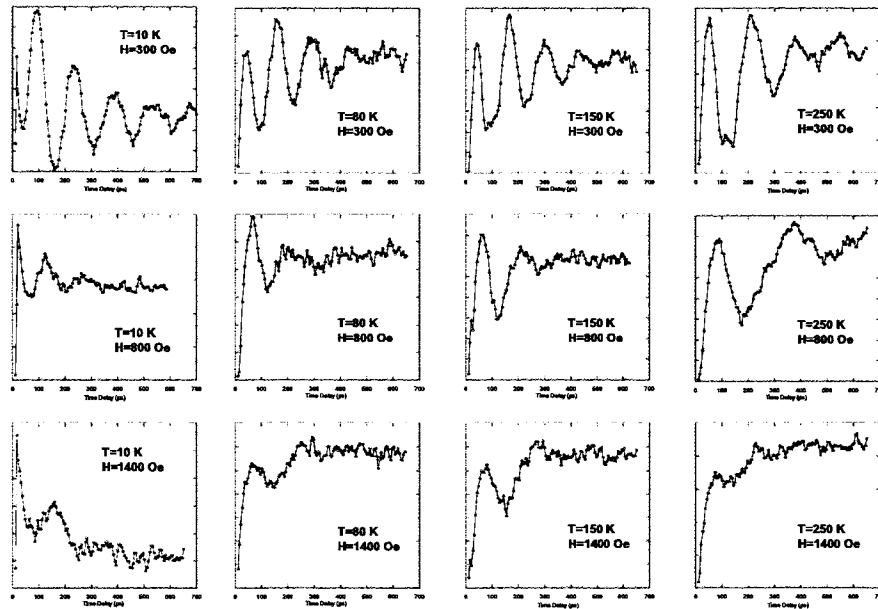


Figure 7.7: Coherent magnetization oscillations as a function of temperature (across, from left to right) and field (down). Notice that the oscillation frequency decreases with temperature. At higher fields, the oscillations can no longer be detected.

In Figure 7.8, the experimental data points below the room temperature and the numerical fittings are shown side by side. Figure 7.9 shows the low temperature data and fittings. There is much larger error (indicated by the larger scatter) in the low temperature data because, as mentioned, the oscillations are not clear, single sinusoidals.

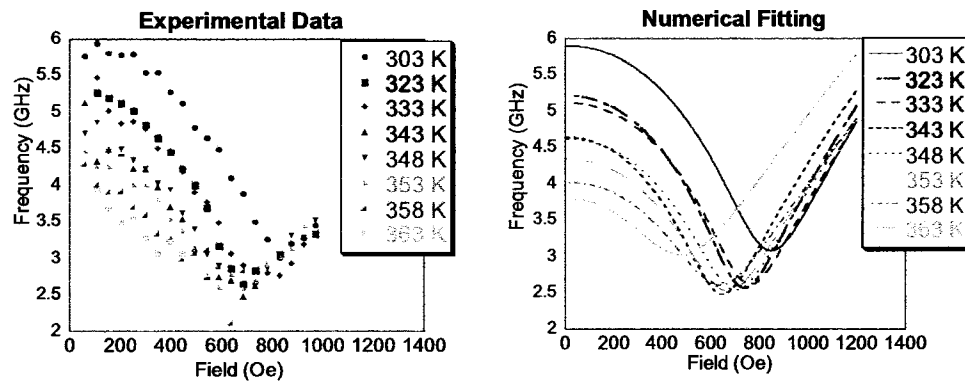


Figure 7.8: Oscillation frequencies as a function of applied field (left) and numerical fits of data including uniaxial and strain anisotropy (right) for the temperature range 303 - 363 K.

To get an idea of the accuracy by which we can extract anisotropy constants from the above data, the error bars for the frequency measurements based on the half widths at half maxima are shown in Figure 7.10, for data taken at 100 K. The center curve is the fit to the data (the center frequencies of the FFTs). The other two lines are numerical fittings to the highest and lowest values of frequency based on the half widths of the FFT.

Among the three fittings, only the center one has a small RMS error, and only the

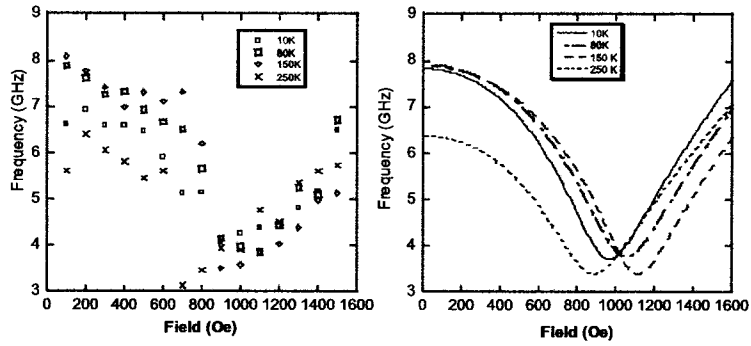


Figure 7.9: Oscillation frequencies as a function of applied field (left) and numerical fits of data including uniaxial and strain anisotropy (right) for the temperature range 10 - 250 K.

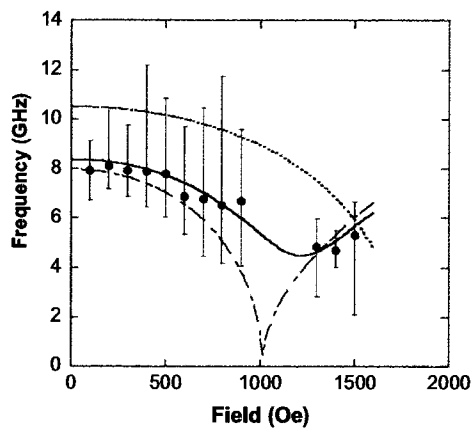


Figure 7.10: Error analysis

center one implies a stress anisotropy K_d . However, the higher one and the lower one give a reasonable uniaxial anisotropy constant K_u that is of the same order of that of the middle one.

| FFT Frequency Fit | K_u (erg/cm ³) | K_δ (erg/cm ³) | RMS (GHz) |
|----------------------|---------------------------------|--------------------------------------|--------------|
| Center | 3.4985×10^5 | 31087 | 0.33898 |
| Lower Half Maximum | 3.2212×10^5 | 0.303 | 1.55106 |
| Higher Half Maximum | 5.5996×10^5 | 0.909 | 1.16524 |

Table 7.2: Error analysis

The values for uniaxial anisotropy and strain anisotropy, along with the RMS error, are summarized in Table 7.3. The errors of K_u and K_d in Table 7.3 are estimated from the RMS values. The values for saturation magnetization are obtained by fitting our high temperature data with equation $M_s = M_0 (1-T/T_c)^{0.371}$, where M_0 is the saturation magnetization at zero temperature [70].

The obtained anisotropy constants at different temperature are displayed in Figure 7.11. It can be observed from the diagrams that the uniaxial anisotropy constant decreases with the temperature and the strain anisotropy constant doesn't change too much. A reasonable thought about the strain anisotropy is it should also decrease with the temperature because the heat can reduce the stress. Possibly, the contribution of the heat isn't big enough to change the lattice mismatch between the sample and the substrate, and this is why we do not see a large observable change of the strain anisotropy constant. The decrease of the uniaxial anisotropy with the temperature is well expected. It was theoretically predicted as a general tendency and also observed in the previous experiments [112, 113, 114, 115, 116].

| Temperature (K) | K_u (erg/cm ³) | K_u Error (erg/cm ³) | K_δ (erg/cm ³) | K_δ Error (erg/cm ³) | RMS (GHz) | M_s (emu/cm ³) |
|--------------------|---------------------------------|---------------------------------------|--------------------------------------|--|--------------|---------------------------------|
| 10 | 2.1792×10^5 | 24450 | 16036 | 1799.2 | 0.6732 | 691.64 |
| 30 | 2.3313×10^5 | 24273 | 18521 | 1928.3 | 0.6247 | 680.03 |
| 40 | 2.2129×10^5 | 17346 | 26697 | 2092.6 | 0.4703 | 674.06 |
| 60 | 2.5211×10^5 | 29896 | 19594 | 2323.6 | 0.7115 | 661.75 |
| 80 | 3.0235×10^5 | 14503 | 21389 | 1026.0 | 0.2878 | 648.91 |
| 100 | 3.4432×10^5 | 35861 | 16007 | 1667.2 | 0.6249 | 635.48 |
| 150 | 3.1227×10^5 | 29083 | 16091 | 1498.6 | 0.5588 | 598.80 |
| 200 | 2.5519×10^5 | 22775 | 14272 | 1273.7 | 0.5355 | 556.29 |
| 250 | 1.7758×10^5 | 15254 | 17520 | 1504.9 | 0.5154 | 504.99 |
| 303 | 1.7323×10^5 | 2527.2 | 16048 | 234.12 | 0.08753 | 433.63 |
| 323 | 1.3403×10^5 | 3487.0 | 10316 | 268.38 | 0.1561 | 398.34 |
| 333 | 1.2758×10^5 | 2587.7 | 10615 | 215.31 | 0.1217 | 377.73 |
| 343 | 1.0615×10^5 | 3106.5 | 10614 | 310.64 | 0.1756 | 354.26 |
| 348 | 1.0312×10^5 | 2119.2 | 10281 | 211.28 | 0.1233 | 341.10 |
| 353 | 89369 | 1992.9 | 9994.2 | 222.87 | 0.1338 | 326.71 |
| 358 | 72225 | 2620.6 | 12098 | 438.96 | 0.2177 | 310.74 |
| 363 | 67854 | 1396.7 | 21222 | 436.82 | 0.1235 | 292.70 |

Table 7.3: Extracted values for uniaxial and strain anisotropy as a function of temperature

There are some interesting features to note in the temperature dependence of the anisotropy as shown in Figure 7.11. First, there is a slight increase in uniaxial anisotropy around 100 K, followed by a decrease (leading to a “bump” at about 100 K in the data). Interestingly, this is around the activation temperature for magnon scattering which produces a noticeable increase in resistivity at about this temperature. The uniaxial anisotropy approaches zero as the temperature approaches the Curie temperature, as expected.

7.5 Summary

In summary of this chapter, we have introduced a new way of measuring magnetic anisotropy constants of CrO₂ by analyzing the optical FMR frequencies of a magnetic

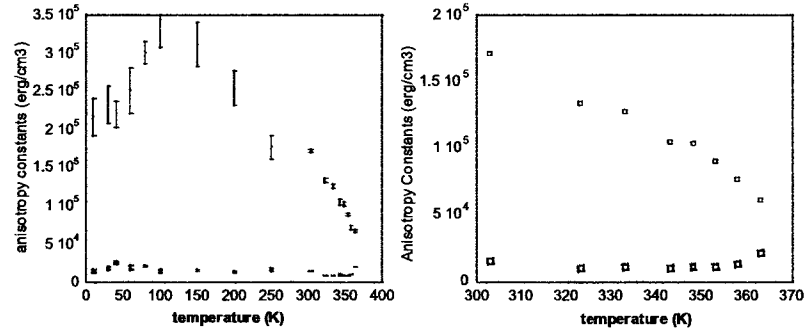


Figure 7.11: Values for uniaxial anisotropy (red) and strain anisotropy (blue) as a function of temperature for 10 - 363 K (left) and an expanded plot from 300 - 363 K (right).

material under the influence of different externally applied field. At room temperature, a value of uniaxial anisotropy was found that is comparable to other measurements. Temperature dependence of the uniaxial anisotropy constant and the strain anisotropy constant of CrO_2 were studied by this all-optical method. The general tendency of our experimental results is consistent with the theoretical prediction and the experimental data obtained by other methods. One interesting feature that was found was an increase in anisotropy around the temperature of 100 K, which corresponds to the onset of magnon scattering and gives rise to the large resistivity increase in CrO_2 .

More work needs to be done to verify the finding of this increase in anisotropy with temperature. First, higher resolution measurements of the oscillation frequency should be attempted. One possibility is to change the orientation of the applied field so it is out of the plane of the sample. Then, larger fields can be accessed since it is

much more difficult to pull the magnetization out of plane. This is the geometry used by Koopmans [13] and more recently Talbayev et al. [117]. Also, the magnetization of our particular sample as a function of temperature should be measured by SQUID magnetometry to compare with the anisotropy values.

Chapter 8

Conclusion

In this thesis we presented our results of ultrafast optical study of half-metallic CrO₂. We have applied ultrafast pump-probe experiments and ultrafast MOKE experiments on thin film CrO₂, and studied electrical and magnetic dynamics of the material. In our pump-probe experiments, optical anisotropy was observed. The obtained ultrafast spectroscopies depend on the polarization of the probe pulses. The wavelength and temperature dependent measurements have implied there is a band gap of 1.5~2 eV near the Fermi surface. All these experimental results are consistent with the Cr3d and O2p hybridization model, which has been proposed by theoretical researchers. The pump-probe experimental results and analysis were presented in Chapter 5. The ultrafast MOKE measurements have been performed to study the spin life time and the magnetic anisotropy of single crystal CrO₂ thin film. Due to the limit of information-noise ratio we can only estimate the spin life time is within several hundreds picoseconds at room temperature. However, the uniaxial anisotropy and the stress anisotropy have been obtained and they are consistent with the results reported by the other researchers. The ultrafast MOKE studies of CrO₂ were reported in Chapter 6 and Chapter 7. In summary, we have shown the ultrafast laser

technique is a powerful tool to study the dynamics of half-metallic materials. For future work, a more sensitive detecting system should be constructed to reduce the noises.

Appendix A

Spectra Physics Laser Systems

A.1 Tsunami

The Tsunami is a cw green laser (Spectra-Physics Millennia) pumped femtosecond Ti:Sapphire laser. The pulse duration is about 120-150 fs with repetition rate of 82 MHz. The wavelength is tunable from 780 nm to 850 nm. In our daily operation, the power is about 600 mW. A schematic of the Tsunami laser cavity is shown below in Figure A.1.

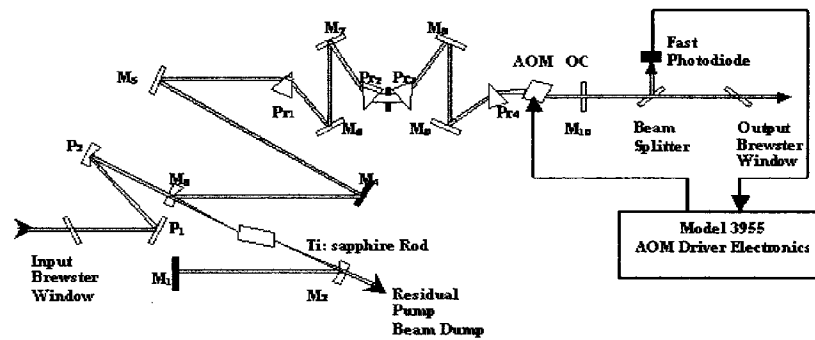


Figure A.1: Spectra-Physics Tsunami

A.2 Spitfire

The Spitfire is a regenerative Ti:Sapphire amplifier pumped by a green laser (Spectra-Physics Evolution) and seeded with the Tsunami. The seed beam is stretched, amplified and compressed to obtain higher peak power. In our daily operation, the average power of Spitfire is 800 mW with a repetition rate of 1 KHz. The pulse duration and the wavelength depend on the seeding, but normally are 150 fs and 800 nm respectively. A schematic of the Spitfire cavity is shown below in Figure A.2.

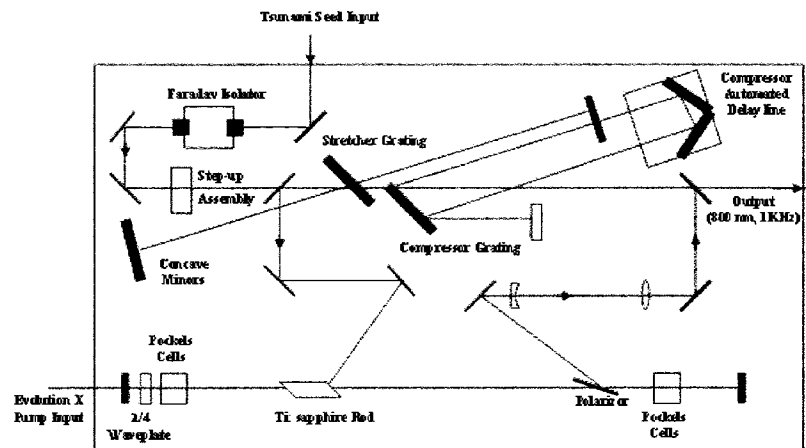


Figure A.2: Spectra-Physics Spitfire

A.3 OPA-800C

The Optical Parametric Amplifier (OPA) is pumped by the output of the Spitfire. The average output power of OPA is about 80 mW for signal and 60 mW for idler, but it is subject to change with the wavelength. The wavelength is tunable from

1140-1600 nm (signal) and 1600-2650 nm (idler). The repetition rate and the pulse duration are about 1 kHz and 150 fs respectively. The basic schematic of the OPA is shown below in Figure A.3.

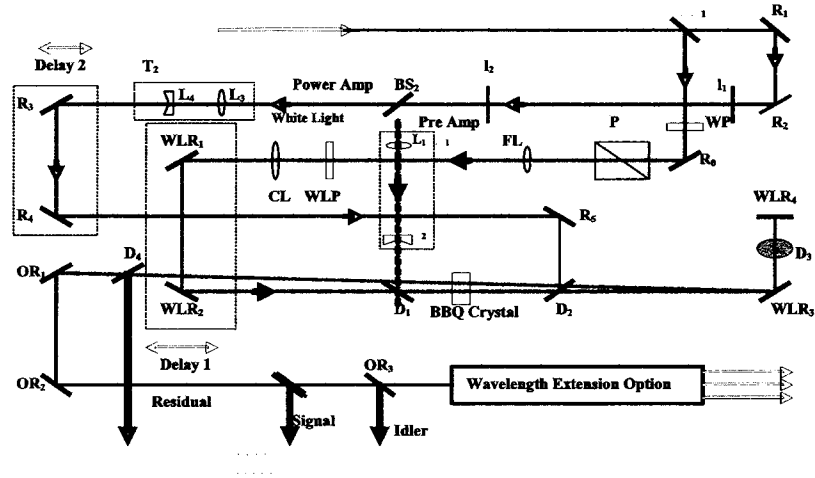


Figure A.3: Spectra-Physics OPA-800C

* The diagrams are due to the courtesy of Yuhang Ren and Ying Wang

Appendix B

Fortran Programs

B.1 Data Fitting

The following program gives the best fitting for anisotropy constants, given the experimental frequency versus field (f-H) data points. It is based on the results of the FMR analysis of the Landau-Lifshitz-Gilbert equations, as described in Chapter 3. Note that the beginning of the program contains the experimental data for field (H) and frequency (f).

```
C      MAIN
      REAL H(20)
      REAL f(20)
      N=20
      H(1)=58.1
      H(2)=106.5
      H(3)=154.8
      H(4)=203.0
      H(5)=251.3
```

$$H(6)=300.5$$

$$H(7)=348.7$$

$$H(8)=396.9$$

$$H(9)=444.9$$

$$H(10)=492.9$$

$$H(11)=541.9$$

$$H(12)=589.8$$

$$H(13)=637.6$$

$$H(14)=685.2$$

$$H(15)=733.0$$

$$H(16)=781.4$$

$$H(17)=828.8$$

$$H(18)=876.2$$

$$H(19)=923.2$$

$$H(20)=970.2$$

$$f(1)=5.7673$$

$$f(2)=5.9419$$

$$f(3)=5.8112$$

$$f(4)=5.7890$$

$$f(5)=5.7939$$

$$f(6)=5.5461$$

$$f(7)=4.5441$$

f(8)=5.2781

f(9)=5.1232

f(10)=4.7850

f(11)=4.6497

f(12)=4.4912

f(13)=4.0998

f(14)=3.8882

f(15)=3.5009

f(16)=3.2618

f(17)=3.0155

f(18)=3.2074

f(19)=3.2749

f(20)=3.4541

CALL READ(Hk1a,Hk1b,Hk2a,Hk2b,Hda,Hdb)

WRITE(*,*) 'Please input number of times to calculate'

READ(*,*) M

DO 70 J=1,M

Hd=(Hda+Hdb)/2.0

dHd=(Hdb-Hda)/2.0

CALL OptimizeHd(Hk1,Hk2,Hd,dHd,H,f,N,x)

Hk1=(Hk1a+Hk1b)/2.0

dHk1=(Hk1b-Hk1a)/2.0

```

        CALL OptimizeHk1(Hk1,dHk1,Hk2,Hd,H,f,N,x)
Hk2=(Hk2a+Hk2b)/2.0
dHk2=(Hk2b-Hk2a)/2.0

        CALL OptimizeHk2(Hk1,Hk2,dHk2,Hd,H,f,N,x)
WRITE(*,*) 'Hk1=',Hk1,' Hk2=',Hk2,' Hd=',Hd
WRITE(*,*) 'G=', x,' number of times calculated',J
70 CONTINUE

END

C SUB1

SUBROUTINE READ(Hk1a,Hk1b,Hk2a,Hk2b,Hda,Hdb)

Hk1a=0

WRITE(*,*) 'Please input upper limit of Hk1'
READ(*,*) Hk1b

Hk2a=0

WRITE(*,*) 'Please input upper limit of Hk2'
READ(*,*) Hk2b

Hda=0

WRITE(*,*) 'Please input upper limit of Hd'
READ(*,*) Hdb

RETURN

END

C SUB2

```

```

SUBROUTINE OptimizeHk1(Hk1,dHk1,Hk2,Hd,Field,Frequency,N,G)

  REAL Field(*)

  REAL Frequency(*)

20      dHk1=dHk1/2.0

  CALL GetG(Hk1,Hk2,Hd,Field,Frequency,N,x)

  G=x

  CALL GetG(Hk1+dHk1,Hk2,Hd,Field,Frequency,N,x)

  Gb=x

  IF (Gb .LT. G) Hk1=Hk1+dHk1

  CALL GetG(Hk1-dHk1,Hk2,Hd,Field,Frequency,N,x)

  Ga=x

  IF (Ga .LT. G) Hk1=Hk1-dHk1

  IF (dHk1 .GT. 0.01) GOTO 20

RETURN Hk1

RETURN G

END

C   SUB3

SUBROUTINE OptimizeHk2(Hk1,Hk2,dHk2,Hd,Field,Frequency,N,G)

  REAL Field(*)

  REAL Frequency(*)

```

```

30          dHk2=dHk2/2.0

          CALL GetG(Hk1,Hk2,Hd,Field,Frequency,N,x)

          G=x

          CALL GetG(Hk1,Hk2+dHk2,Hd,Field,Frequency,N,x)

          Gb=x

          IF (Gb .LT. G) Hk2=Hk2+dHk2

          CALL GetG(Hk1,Hk2-dHk2,Hd,Field,Frequency,N,x)

          Ga=x

          IF (Ga .LT. G) Hk2=Hk2-dHk2

          IF (dHk2 .GT. 0.001) GOTO 30

          RETURN Hk2

          RETURN G

          END

C          SUB4

          SUBROUTINE OptimizeHd(Hk1,Hk2,Hd,dHd,Field,Frequency,N,G)

          REAL Field(*)

          REAL Frequency(*)

40          dHd=dHd/2.0

          CALL GetG(Hk1,Hk2,Hd,Field,Frequency,N,x)

          G=x

          CALL GetG(Hk1,Hk2,Hd+dHd,Field,Frequency,N,x)

          Gb=x

```

```

        IF (Gb .LT. G) Hd=Hd+dHd

        CALL GetG(Hk1,Hk2,Hd-dHd,Field,Frequency,N,x)

        Ga=x

        IF (Ga .LT. G) Hd=Hd-dHd

    IF (dHd .GT. 0.1) GOTO 40

    RETURN Hd

    RETURN G

    END

C   SUB5

    SUBROUTINE GetG(Hk1,Hk2,Hd,Field,Frequency,N,G)

        REAL Field(*)

        REAL Frequency(*)

        x=0.0

    DO 50 I=1,N

        CALL SOLVE(Hk1,Hk2,Hd,Field(I),ff)

            x=x+(Frequency(I)-ff)*(Frequency(I)-ff)

50    CONTINUE

        G=SQRT(x)

    RETURN G

    END

C   SUB6

    SUBROUTINE SOLVE(Hk1,Hk2,Hd,H,ff)

```

```

A=(1.0/2.0)*SQRT(Hk1*Hk1+Hk2*Hk2)
s=ASIN(Hk2/2/A)
pi=3.1415926
p1=0
p2=pi/2
60      dp=p2-p1
p=p1+dp/2
F=A*sin(2*p-s)-H*cos(p)
IF (F .LT. 0) p1=p
IF (F .GT. 0) p2=p
IF (F .EQ. 0) GOTO 70
If (dp .GT. 0.000001) Goto 60
70 ff=0.0176/2/pi*SQRT((H*sin(p)+Hd)*(H*sin(p)+Hk1*cos(2*p)+Hk2*sin(2*p)))
RETURN ff
END

```

B.2 Recovering

The following program plots the f-H curve, given the anisotropy constants and other experimental details.

```
C    MAIN
```

```

REAL Hk1,Hk2,Hd,Hmax,dH,pp
WRITE(*,*) 'Please input the Field-EasyAxis Angle'

READ(*,*) pp

WRITE(*,*) 'Please input Hk1'

READ(*,*) Hk1

WRITE(*,*) 'Please input Hk2'

READ(*,*) Hk2

WRITE(*,*) 'Please input Hd'

READ(*,*) Hd

WRITE(*,*) 'Please input the maximum field you want to go'

READ(*,*) Hmax

WRITE(*,*) 'Please input the number of data points you want to have'

READ(*,*) N

dH=Hmax/N

DO 20 I=1, N

H=I*dH

A=(1.0/2.0)*SQRT(Hk1*Hk1+Hk2*Hk2)

s=ASIN(Hk2/2/A)

pi=3.1415927

p1=0

p2=pi/2

10          dp=p2-p1

```

```

p=p1+dp/2

F=A*sin(2*p-s)+H*sin(p-pp*pi/180.0)

IF (F .LT. 0.00000) p1=p

IF (F .GT. 0.00000) p2=p

IF (F .EQ. 0.00000) GOTO 30

If (dp .GT. 0.000001) Goto 10

30      ff=H*cos(p-pp*pi/180.0)

ff=0.0176/2/pi*SQRT(((ff+Hd)*(ff+Hk1*cos(2*p)+Hk2*sin(2*p))))

Angle=p*180.0/pi

Write(*,*) H,ff,Angle

20      continue

END

```

Bibliography

- [1] K. Schwarz. *Journal of Physics F: Metal Physics*, 16:211, 1986.
- [2] K. P. Kämper, W. Schmitt, G. Güntherodt, R. J. Gambino, and R. Ruf. *Physical Review Letters*, 59:2788, 1987.
- [3] Y. Ji, G. J. Strijkers, F. Y. Yang, C. L. Chien, J. M. Byers, A. Anguelouch, G. Xiao, and A. Gupta. *Physical Review Letters*, 86:5585, 2001.
- [4] E. J. Singley, C. P. Weber, D. N. Basov, A. Barry, and J. M. D. Coey. *Physical Review B*, 60:4126, 1999.
- [5] S. M. Watts, S. Wirth, S. von Molnär, A. Barry, and J. M. D. Coey. *Physical Review B*, 61:9621, 2000.
- [6] M. Julliere. *Physics Letters A*, 54:225, 1975.
- [7] W. Pickett and J. Moodera. *Physics Today*, 54:39, 2001.
- [8] J. R. Goldman and J. A. Prybyla. *Physical Review Letters*, 72:1364, 1993.
- [9] A. C. Schaefer and D. G. Steel. *Physical Review Letters*, 79:4870, 1997.
- [10] R. W. Schoenlein, W. Z. Lin, J. G. Fujimoto, and G. L. Eesley. *Physical Review Letters*, 58:1680, 1987.
- [11] T. Kise, T. Ogasawara, M. Ashida, Y. Tomioka, Y. Tokura, and M. Kuwata-Gonokami. *Physical Review Letters*, 85:1986, 2000.
- [12] Q. Zhang, A. V. Nurmikko, A. Anguelouch, G. Xiao, and A. Gupta. *Physical Review Letters*, 89:177402, 2002.
- [13] M. van Kampen, C. Jozsa, J. T. Kohlhepp, P. LeClair, L. Lagae, W. J. M. de Jonge, and B. Koopmans. *Physical Review Letters*, 88:227201, 2002.
- [14] R. D. Averitt and A. J. Taylor. *Journal of Physics: Condensed Matter*, 14:R1357, 2002.
- [15] E. Beaurepaire, J.-C. Merle, A. Daunois, and J.-Y. Bigot. *Physical Review Letters*, 76:4250, 1996.

- [16] J. Hohlfeld, E. Mathias, R. Knorren, and K. H. Bennemann. *Physical Review Letters*, 78:4861, 1997.
- [17] Ganping Ju, A. Vertikov, A. V. Nurmikko, C. Canady, G. Xiao, R. F. C. Farrow, and A. Cebollada. *Physical Review B*, 57:R700, 1998.
- [18] W. K. Hiebert, A. Stankiewicz, and M. R. Freeman. *Physical Review Letters*, 79:1134, 1997.
- [19] J. P. Park, P. Eames, D. M. Engebretson, J. Berezovsky, and P. A. Crowell. *Physical Review Letters*, 89:277201, 2002.
- [20] R. A. de Groot, F. M. Mueller, P. G. van Engen, and K. H. J. Buschow. *Physical Review Letters*, 50:2024, 1983.
- [21] E. Kulatov and I. I. Mazin. *Journal of Physics: Condensed Matter*, 2:343, 1990.
- [22] S. P. Lewis, P. B. Allen, and T. Sasaki. *Physical Review B*, 55:10253, 1997.
- [23] M. A. Korotin, V. I. Anisimov, D. I. Khomskii, and G. A. Sawatzky. *Physical Review Letters*, 80:4305, 1998.
- [24] I. I. Mazin, D. J. Singh, and C. Ambrosch-Draxl. *Physical Review B*, 59:411, 1999.
- [25] H. Y. Hwang and S. W. Cheong. *Science*, 278:1607, 1997.
- [26] J. M. D. Coey, A. E. Berkowitz, L. Balcells, F. F. Putris, and A. Barry. *Physical Review Letters*, 80:3815, 1998.
- [27] Y. S. Dedkov, M. Fonine, C. König, U. Rüdiger, G. Gütherodt, S. Senz, and D. Hesse. *Applied Physics Letters*, 80:4181, 2002.
- [28] H. Huang, K. Seu, A. Reilly, Y. Kadmon, and W. F. Egelhoff Jr. *Journal of Applied Physics*, 97, 2005.
- [29] K. E. H. M. Hanssen, P. E. Mijnders, L. P. L. M. Rabou, and K. H. J. Buschow. *Physical Review B*, 42:1533, 1990.
- [30] M. Pénicaud, B. Siberchicot, C. B. Sommers, and J. Kübler. *Journal of Magnetism and Magnetic Materials*, 103:212, 1992.
- [31] S. F. Alvarado, W. Eib, F. Meier, D. T. Pierce, K. Sattler, and H. C. Siegmann. *Physical Review Letters*, 34:319, 1975.
- [32] W. Pickett and D. J. Singh. *Physical Review B*, 53:1146, 1996.
- [33] B. Nadgorny, I. I. Mazin, M. Osofsky, R. J. Soulen Jr., P. Broussard, R. M. Stroud, D. J. Singh, V. G. Harris, A. Arsenov, and Ya. Mukovskii. *Physical Review B*, 63:184433, 2001.

- [34] J. H. Park, E. Vescovo, H. J. Kim, C. Kwon, R. Ramesh, and T. Venkatesan. *Nature*, 392:794, 1998.
- [35] K. I. Kobayashi, T. Kimura, H. Sawada, K. Terakura, and Y. Tokura. *Nature*, 395:677, 1998.
- [36] Y. Q. Xu, B. G. Liu, and D. G. Pettifor. *Physical Review B*, 66:184435, 2002.
- [37] I. I. Mazin. *Applied Physics Letters*, 77:3000, 2000.
- [38] S. F. Cheng, G. T. Woods, K. Bussmann, I. I. Mazin, R. J. Soulen Jr., E. E. Carpenter, B. N. Das, and P. Lubitz. *Journal of Applied Physics*, 93:6847, 2003.
- [39] T. Ogawa, M. Shirai, N. Suzuki, and I. Kitagawa. *Journal of Magnetism and Magnetic Materials*, 196-197:428, 1999.
- [40] J. G. Braden, J. S. Parker, P. Xiong, S. H. Chun, and N. Samarth. *Physical Review Letters*, 91:056602, 2003.
- [41] V. Yu. Irkhin and M. I. Katsnelson. *European Physical Journal B*, 30:481, 2002.
- [42] A. Gupta and J. Z. Sun. *Journal of Magnetism and Magnetic Materials*, 200:24, 1999.
- [43] J. Kübler. *Physical Review B*, 67:220403, 2003.
- [44] S. J. Hashemifar, P. Kratzer, and M. Scheffler. *Physical Review Letters*, 94:096402, 2005.
- [45] R. J. Soulen Jr., J. M. Byers, M. S. Osofsky, B. Nadgorny, T. Ambrose, S. F. Cheng, P. R. Broussard, C. T. Tanaka, J. Nowak, J. S. Moodera, A. Barry, and J. M. D. Coey. *Science*, 282:85, 1998.
- [46] R. J. Soulen Jr., M. S. Osofsky, B. Nadgorny, T. Ambrose, P. Broussard, S. F. Cheng, J. Byers, C. T. Tanaka, J. Nowack, J. S. Moodera, G. Laprade, A. Barry, and J. M. D. Coey. *Journal of Applied Physics*, 85:4589, 1999.
- [47] J. M. D. Coey and C. L. Chien. *MRS Bulletin/October*, 2003.
- [48] P. A. Dowben and R. Skomski. *Journal of Applied Physics*, 95:7453, 2004.
- [49] W. Pickett. *Physical Review B*, 57:10613, 1998.
- [50] R. Weht and W. Pickett. *Physical Review B*, 60:13006, 1999.
- [51] R. Wiesendanger, H. J. Güntherodt, G. Güntherodt, R. J. Gambino, and R. Ruf. *Physical Review Letters*, 65:247, 1990.
- [52] C. M. Fu, C. J. Lai, J. S. Wu, J. C. A. Huang, C. C. Wu, and S. G. Shyu. *Journal of Applied Physics*, 89:7702, 2001.

- [53] J. S. Parker, P. G. Ivanov, D. M. Lind, P. Xiong, and Y. Xin. *Physical Review B*, 69:220413, 2004.
- [54] C. B. Stagaescu, X. Su, D. E. Eastman, K. N. Altmann, F. J. Himpsel, and A. Gupta. *Physical Review B*, 61:9233, 2000.
- [55] L. L. Chase. *Physical Review B*, 10:2226, 1974.
- [56] M. van Veenendaal and A. J. Fedro. *Physical Review B*, 70:012412, 2004.
- [57] N. E. Brener, J. M. Tyler, J. Callaway, D. Bagayoko, and G. L. Zhao. *Physical Review B*, 61:16582, 2000.
- [58] L. Craco, M. S. Laad, and E. Müller-Hartmann. *Physical Review Letters*, 90:237203, 2003.
- [59] A. Toropova, G. Kotliar, S. Y. Savrasov, and V. S. Oudovenko. *arXiv:cond-mat/0409554*, 2004.
- [60] P. Schlottmann. *Physical Review B*, 67:174419, 2003.
- [61] M. N. Iliev, A. P. Litvinchuk, H. G. Lee, C. W. Chu, A. Barry, and J. M. D. Coey. *Physical Review B*, 60:33, 1999.
- [62] R. Vidya, P. Ravindran, A. Kjekshus, and H. Fjellvåg. *Physical Review B*, 70:184414, 2004.
- [63] H. Brändle, D. Weller, S. S. Parkin, J. C. Scott, P. Fumagalli, W. Reim, R. J. Gambino, R. Ruf, and G. Güntherodt. *Physical Review B*, 46:13889, 1992.
- [64] Y. A. Uspenskii, E. T. Kulatov, and S. V. Halilov. *Physical Review B*, 54:474, 1996.
- [65] J. Kuneš, P. Novák, P. M. Oppeneer, C. König, M. Fraune, U. Rüdiger, G. Güntherodt, and C. Ambrosch-Draxl. *Physical Review B*, 65:1651XX, 2002.
- [66] H. van Leuken and R. A. de Groot. *Physical Review B*, 51:7176, 1995.
- [67] X. W. Li, A. Gupta, T. R. McGuire, P. R. Duncombe, and G. Xiao. *Journal of Applied Physics*, 85:5585, 1999.
- [68] A. Anguelouch, A. Gupta, G. Xiao, D. W. Abraham, Y. Ji, S. Ingvarsson, and C. L. Chien. *Physical Review B*, 64:180408, 2001.
- [69] J. S. Kouvel and D. S. Rodbell. *Physical Review Letters*, 18:215, 1967.
- [70] F. Y. Yang, C. L. Chien, X. W. Li, G. Xiao, and A. Gupta. *Physical Review B*, 63:092403, 2001.

- [71] L. Ranno, A. Barry, and J. M. D. Coey. *Journal of Applied Physics*, 81:5774, 1997.
- [72] A. Barry, J. M. D. Coey, L. Ranno, and K. Ounadjela. *Journal of Applied Physics*, 83:7166, 1998.
- [73] R. Yamamoto, Y. Moritomo, and A. Nakamura. *Physical Review B*, 61:5062, 2000.
- [74] M. S. Laad, L. Craco, and E. Müller-Hartmann. *Physical Review B*, 64:214421, 2001.
- [75] D. J. Huang, H. T. Jeng, C. F. Chang, G. Y. Guo, J. Chen, W. P. Wu, S. C. Chung, S. G. Shyu, C. C. Wu, H. J. Lin, and C. T. Chen. *Physical Review B*, 66:174440, 2002.
- [76] E. Goering, A. Bayer, S. Gold, G. Schütz, M. Rabe, U. Rüdiger, and G. Güntherodt. *Physical Review Letters*, 88:207203, 2002.
- [77] M. Komelj, C. Ederer, and M. Fähnle. *Physical Review B*, 69:132409, 2004.
- [78] D. J. Huang, L. H. Tjeng, J. Chen, C. F. Chang, W. P. Wu, S. C. Chung, A. Tanaka, G. Y. Guo, H. J. Lin, S. G. Shyu, C. C. Wu, and C. T. Chen. *Physical Review B*, 67:214419, 2003.
- [79] E. Z. Kurmaev, A. Moewes, S. M. Butorin, M. I. Katsnelson, L. D. Finkelstein, J. Nordgren, and P. M. Tedrow. *Physical Review B*, 67:155105, 2003.
- [80] F. Y. Yang, C. L. Chien, E. F. Ferrari, X. W. Li, G. Xiao, and A. Gupta. *Applied Physics Letters*, 77:286, 2000.
- [81] I. L. Siu, W. F. Egelhoff Jr., D. X. Yang, and H. D. Chopra. *Journal of Applied Physics*, 92:5409, 2002.
- [82] X. W. Li, A. Gupta, and G. Xiao. *Applied Physics Letters*, 75:713, 1999.
- [83] L. Spinu, H. Srikanth, A. Gupta, X. W. Li, and G. Xiao. *Physical Review B*, 62:8931, 2000.
- [84] P. A. Stampe, R. J. Kennedy, S. M. Watts, and S. von Molnaár. *Journal of Applied Physics*, 89:7696, 2001.
- [85] P. Lubitz, M. Rubinstein, M. S. Osofsky, B. E. Nadgorny, R. J. Soulen, K. M. Bussmann, and A. Gupta. *Journal of Applied Physics*, 89:6695, 2001.
- [86] B. Z. Rameev, R. Yilgin, B. Aktas, A. Gupta, and L. R. Tagirov. *Microelectronic Engineering*, 69:336, 2003.
- [87] Y. Ren. The college of william and mary. *Ph. D. Dissertation*, 2003.

- [88] Weizhu Lin, Robert W. Schoenlein, and James G. Fujimoto. *IEEE Journal of Quantum Electronics*, 24:267, 1988.
- [89] V. V. Kabanov, J. Demsar, B. Podobnik, and D. Mihailovic. *Physical Review B*, 59:1497, 1999.
- [90] Y. J. Yan, L. E. Fried, and S. Mukamel. *Journal of Physical Chemistry*, 93:8149, 1989.
- [91] K. H. Bennemann. *Nonlinear Optics of Metals*, (Oxford University Press, Oxford), 1999.
- [92] J. L. Erskine and E. A. Stern. *Physical Review B*, 12:5016, 1975.
- [93] H. S. Bennett and Edward A. Stern. *Physical Review*, 137:A448, 1965.
- [94] P. N. Argyres. *Physical Review*, 97:334, 1955.
- [95] R. Hunt. *Journal of Applied Physics*, 38:1652, 1967.
- [96] C. You and S. Shin. *Applied Physics Letters*, 69:1351, 1996.
- [97] J. C. Anderson. *Magnetism and Magnetic Materials*, (Chapman and Hall LTD., London), 1968.
- [98] G. V. Skrotskii and L. V. Kurbatov. *Ferromagnetic Resonance*, (Pergamon, Oxford), 1966.
- [99] P. G. Ivanov, S. M. Watts, and D. M. Lind. *Journal of Applied Physics*, 89:1035, 2001.
- [100] B. J. Thamer, R. M. Douglass, and E. Staritzky. *Journal of the American Chemical Society*, 79:547, 1957.
- [101] R. D. Averitt, A. I. Lobad, C. Kwon, S. A. Trugman, V. K. Thorsmølle, and A. J. Taylor. *Physical Review Letters*, 87:017401, 2001.
- [102] S. Chiczumi. *Physics of magnetism*. New York: John Wiley & Sons, 1964.
- [103] G. A. Prinz. *Science*, 282:1660, 1998.
- [104] S. A. Wolf, D. D. Awschalom, R. A. Buhrman, J. M. Daughton, S. von Molnár, M. L. Roukes, A. Y. Chtchelkanova, and D. M. Treger. *Science*, 294:1488, 2001.
- [105] Jagadeesh S. Moodera and G. Mathon. *Journal of Magnetism and Magnetic Materials*, 200:248, 1999.
- [106] J. Fabian and S. D. Sarma. *Journal of Vacuum Science and Technology B*, 17:1708, 1999.

- [107] M. van Kampen. Technische universiteit eindhoven. *Ph. D. Dissertation*, 2003.
- [108] J. Araya-Pochet, C. A. Ballentine, and J. L. Erskine. *Physical Review B*, 38:7846, 1988.
- [109] M. Kowalewski, C. M. Schneider, and B. Heirich. *Physical Review B*, 47:8748, 1993.
- [110] M. C. Smoak, P. A. Ryan, F. Tsui, T. K. Nath, R. A. Rao, D. Lavric, and C. B. Eom. *Journal of Applied Physics*, 87:6764, 2000.
- [111] O. Heczko, L. Straka, N. Lanska, K. Ullakko, and J. Enkovaara. *Journal of Applied Physics*, 91:8228, 2002.
- [112] Y. Millev and M Fähnle. *Physical Review B*, 51:2937, 1995.
- [113] Y. Millev and M Fähnle. *Physical Review B*, 52:4336, 1995.
- [114] D. Sander. *Journal of Physics: Condensed Matter*, 16:R603, 2004.
- [115] C. Zener. *Physical Review*, 96:1335, 1954.
- [116] R. Brenner. *Physical Review*, 107:1539, 1957.
- [117] D. Talbayev, H. Zhao, G. Lüpke, J. Chen, and Q. Li. *Applied Physics Letters*, 86:182501, 2005.

VITA

Hailong Huang

Mr. Hailong Huang was born on June 3, 1979, in Fengxin, Jiangxi Province, China. He received his B. S. in physics from Jilin University in 1998. He started his graduate studies at the College of William and Mary in 2000, and was supported by research assistantship from Prof. Anne C. Reilly. The author received his M. S. in physics in 2001.